DISSERTATION

TURNING NIGHT INTO DAY: THE CREATION, VALIDATION, AND APPLICATION OF SYNTHETIC LUNAR REFLECTANCE VALUES FROM THE DAY/NIGHT BAND AND INFRARED SENSORS FOR USE WITH JPSS VIIRS AND GOES ABI.

Submitted by

Chandra M. Pasillas

Department of Atmospheric Science

In partial fulfillment of the requirements

For the Degree of Doctor of Philosophy

Colorado State University

Fort Collins, Colorado

Spring 2023

Doctoral Committee:

Advisor: Christian Kummerow
Co-Advisor: Michael Bell

Steven D. Miller
Kristen Rasmussen
Steven Reising

ABSTRACT

TURNING NIGHT INTO DAY: THE CREATION, VALIDATION, AND APPLICATION OF SYNTHETIC LUNAR REFLECTANCE VALUES FROM THE DAY/NIGHT BAND AND INFRARED SENSORS FOR USE WITH JPSS VIIRS AND GOES ABI.

Satellite remote sensing revolutionized weather forecasting and observing in the 1960s providing a true bird's eye view of the weather beyond what could be achieved from balloon and aircraft reconnaissance. With advances in observing systems came the desire for more capabilities and a better understanding of the Earth system, leading to rapid increases in satellite imaging capabilities. The most popular imager products come from solar reflective radiation in the form of visible imagery as they are the most intuitive to users. Similar benefits were later made possible by equivalent nighttime imagery; first available through the Operational Linescan System (OLS) and then the Day/Night Band (DNB), but these sensors have limited revisit time due to their low Earth orbits. A day-night band sensor in geostationary orbit would greatly enhance the utility of this measurement for nowcasters, but it does not exist. Work towards a pseudo-nighttime visible imagery to fill this gap has been done with varying results (Chirokova et al., 2018; Kim et al., 2019; Kim and Hong, 2019; Mohandoss et al., 2020; Harder et al., 2020). This dissertation demonstrates the creation and implementation of a machine learning model to turn night into day by transforming satellite radiance observations into representative full moon lunar reflectance values that provide quantifiable metrics and visible-like imagery to its users.

In Chapter 2, a method is described that utilizes a feed-forward neural network model to replicate DNB lunar reflectance using brightness temperatures and brightness temperature differences in the short and long-wave infrared (IR) spectrum as the primary input. The goal was to improve upon the performance of the DNB during new moon periods, and lay the foundation for transitioning the algorithm to the Geostationary Operational Environmental Satellite (GOES) Advanced

Baseline Imager (ABI). Results from this method are the first to quantitatively validate low-light visible nighttime imagery with lunar reflectance calculated from DNB radiances. This work further demonstrated that there is a relationship between full moon lunar reflectance and IR that can be captured to create imagery that is visually consistent across the full lunar cycle regardless of moon phase and angle.

In Chapter 3, the machine learning (ML) nighttime visible imagery (NVI) model is applied to the GOES ABI utilizing wavelength relationships and satellite inter-calibrations information. This demonstrates that a model trained and validated on VIIRS polar orbiting imagery can work on sensors aboard geostationary satellites. It also confirms why the 10.3 μm channel is the preferred substitution for the 10.7 μm centered band over the 11.2 μm channel. Furthermore, it demonstrates that lunar reflectance derived from IR can be replicated across sensors with similar spectral response functions providing enhanced geographic and temporal resolution that is not possible on the JPSS platforms.

The final section of the dissertation transitions into forecaster applications by examining case studies concerning tropical cyclones and fog in greater detail. Focused on low cloud detection, NVI provides additional information not possible from IR and current analysis products available. It can detect tropical cyclone low-level circulations through cirrus cloud and identify fog extent more readily. The findings in this doctoral study will advance remote sensing of clouds at night, further reducing weather now-casting errors and increasing weather-related safety.

ACKNOWLEDGEMENTS

I would like to thank both my advisors, Dr. Christian Kummerow and Dr. Michael Bell, for taking a chance on a non-traditional student such as myself; they believed in me at times when I did not. Also all the members of the K-group and Bell group members for their patience and friendship. Dr. Jason Patla, thank you for encouraging me to apply and reapply to the Air Force PhD program, without your guidance I would be on a very different career path. Cole Fredrick, you were instrumental in getting my coding skills up to survivable, I thank you. I would also like to thank my friends and family who helped me see this to completion. Finally, to Diana, luckily you will not remember much about the long days and hours I spent at the computer when I would have much rather been playing with you, but I thank you for your understanding and for keeping me company many times in my home office doing crafts, coloring, and learning while I worked.

DEDICATION

I would like to dedicate this dissertation to my daughter Diana, you are my light and motivation. I will love you always.

TABLE OF CONTENTS

ABSTRACT ii
ACKNOWLEDGEMENTS iv
DEDICATION v
LIST OF TABLES vii
LIST OF FIGURES viii

Chapter 1 Introduction 1
1.1 Motivation 1
1.2 Objectives and Outline of Dissertation 2

Chapter 2 Turning Night Into Day: The Creation and Validation of Synthetic Night-time Visible Imagery Using the Joint Polar Satellite System (JPSS) Day/Night Band (DNB) and Machine Learning 4
2.1 Introduction 4
2.2 Data 12
2.3 Model Architecture and Training 15
2.4 VIIRS Validation and Results 17
2.5 Discussion and Conclusion 26

Chapter 3 Improving Data Latency for Nighttime Visible Imagery: Transitioning Night-time Visible Imagery from the JPSS VIIRS to the GOES ABI 32
3.1 Introduction 32
3.2 Data 36
3.3 Machine Learning and Architecture 39
3.4 GOES ABI Validation 40
3.5 Demonstration of Forecasting Uses for A-NVI 45
3.6 Summary and Conclusion 48

Chapter 4 Improving the A-NVI and applications 51
4.1 Introduction 51
4.2 Creation and General Uses for Nighttime Visible Imagery 52
4.3 Cases 53
4.3.1 Tropical Cyclones 53
4.3.2 Fog 56
4.4 Conclusions and Future Work 58

LIST OF TABLES

2.1 List of Predictors used in the VIIRS ML-NVI creation, associated central wavelengths or wavelength differences, wavelength range, and associated prior research applications. 14
2.2 Training iterations for the FNN used to determine the preferred model set- up. Models with 40 epochs and a batch size of 2048 performed the most consistently regardless of the latitude associated with the training or validation data. 17
2.3 A consolidation of the validation metrics for the full-latitude model across all three validation regions. Scores for the full-latitude model in the 0N-50N AOI demonstrate model performance for use of a singular global model across all seasons. 25

3.1 VIIRS moderate band central wavelengths and brightness temperature differences with the corresponding ABI bands central wavelengths and brightness temperatures differences used in training and validating the nighttime visible imagery (NVI). Previous research conducted for cloud detection on the brightness temperature differences is provided in the far right column. 39
3.2 Quantitative metrics for the 2020 validations area of interest for the V-NVI, C13 A-NVI, and C14 A-NVI (left to right). 45

LIST OF FIGURES

2.1 Observed infrared spectrum and absorption gases by spectral location from a high-resolution interferometer sounder (L) and brightness temperature spectra from a high-resolution infrared spectrometer indicating wavelength-dependent brightness temperature changes by cloud type (R). Figure taken directly from Liou (2002) 4.3 and 4.12. . 6
2.2 Area of Interest (AOI) for the study was a bounding box 50N, 0N, 125W, 180W. AOI was further divided into two subregions at 30N. Base map modified from https://web.ics.purdue.edu/ braile/edumod/epiplot/epiplot.htm 13
2.3 AI Architecture for the ML-NVI. ML Architecture consists of 10 inputs, 2 hidden layers with 8 nodes, 1 hidden layer with 4 nodes; all with an Adam optimizer, MSE loss function, and RelU activation functions; and a single node output layer using the Sigmoid activation function. Training data was then processed through the model for 40 Epochs with a batch size of 2048. 16
2.4 Qualitative Comparisons (Left to Right) of images from DNB radiance calculated lunar reflectance, predicted lunar reflectance for the three latitudinal models (Full-latitude, Low-latitude, Mid-latitude), and VIIRS M13 (4.05 μm) and M16 (12.01 μm) sensors. The top two rows highlight general cloud features, the middle two rows are fog events, and the bottom two rows are a tropical storm event. 19
2.5 Probability Density Functions of the three latitudinal model lunar reflectance distributions versus the true DNB lunar reflectance distribution for the 0N-50N validation AOI. 22
2.6 Qualitative Comparisons (Left to Right) of images from DNB radiance calculated lunar reflectance, predicted lunar reflectance, lunar reflectance differences between truth and predicted values, and VIIRS 12.01 μm channel for various scenes. 29
2.7 Qualitative Imagery Comparisons (Left to Right) of True DNB Lunar Reflectance, Full-Latitude Model Lunar Reflectance, and sensor radiances for VIIRS M13 (4.05 μm) and M16 (12.01 μm) for May 25, 2000 - July 18, 2000 covering 1.5 lunar cycles with high illumination present in rows 2,6,7. 30
2.8 Lunar Reflectance Comparisons. Left: Data comparison of the 2020 validation data and the DNB true lunar reflectance for the full latitude VIIRS model over the 0N-50N AOI. Right: DNB true lunar reflectance minus full-latitude model reflectance evaluated at 0N-50N AOI. 31

3.1 Depiction of the GOES 17 ABI sensor footprint and associated pixel size for the full disk, CONUS, and mesoscale scenes. The black box highlights the study area of interest. Figure modified from (Schmit et al., 2017) Fig 5. 37
3.2 MODTRAN standard atmosphere profile from 3-14 μm with spectral response functions for the JPSS VIIRS (orange) and GOES ABI (blue) channels overlaid. 38
3.3 Model Architecture for the Nighttime Visible Imagery (NVI) 41
3.4 Qualitative comparison for the 2020 GOES ABI Nighttime Visible Imagery Validation. For each case, from left to right are the DNB true lunar reflectance, V-NVI, C13 A-NVI, C14 A-NVI, ABI Channel 07 (3.9 μm), and ABI Channel 15 (12.3 μm). 42

3.5 Normalized lunar reflectance values for the observed lunar reflectance (grey), VIIRS-NVI (blue), C13 A-NVI (red), and C14 A-NVI (green) over the ABI-NVI validation area of interest. 43
3.6 Scatter plots of the observed vs A-NVI predicted lunar reflectance(left) and histogram of the observed minus predicted lunar reflectance(right). 44
3.7 Qualitative comparisons for Tropical Cyclone Ema between true lunar reflectance, V-NVI, M15 (top row, left to right) and ABI channel 07, A-NVI, and ABI channel 15 (bottom row, left to right) to highlight footprint and wavelength resolution differences. 46
3.8 Qualitative comparisons between ABI channel 07 (3.9 µm), A-NVI, and ABI channel 15 (12.3 µm)(left to right) at mesoscale (row 1 and 2) and CONUS scale (row 3 and 4) view points. 50

4.1 Hurricane Otis comparisons of ABI channel C07 (3.9µm), A-NVI, and ABI channel C15 (12.3µm)(left to right) leading to tropical depression declaration at times 10/12Z 11/00Z 11/03Z/ 11/06Z and 11/09Z (top to bottom) 62
4.2 Hurricane Otis comparisons of ABI channel C07 (3.9 µm), C13 A-NVI, GOES+ A-NVI and ABI channel C15 (12.3 µm) (left to right) at times 17/04Z, /17/07Z, and 17/10Z (top to bottom) leading to category 1 hurricane declaration. 63
4.3 Map of the sensor locations in the area of interest (top) and ceiling and visible coding for Instrument Flight Rules (red), Marginal Visual Flight Rules (yellow), Visual Flight Rules (white), and potential M/IFR (blue) observations by hour from 02Z-16Z for the event.) 64
4.4 Comparisons for 28 January 2023 fog case at 03Z (top set), 09Z (middle set), and 15Z (bottom set) for A-NVI and current forecasting imagery.) 65

Chapter 1

Introduction

1.1 Motivation

On July 20, 1969, history was made when man landed on the moon. Four days later the command module returned, and the success of Apollo 11 was celebrated. This mission could have had a much more tragic ending had Air Force Captain Henri Brandli not been tracking clouds in support of military aerial photography reconnaissance via a secret military weather satellite program later known as the Defense Meteorological Satellite Program (DMSP). He noticed significant storms developing near the recovery site and was bold enough to act (McCormack, 2019). This was not the first time weather played a key role in history nor would it be the last, however, it proves the criticality of having access to earth observing systems from space in the form of satellites to monitor weather for the preservation of life and the importance of cooperation between civilian, military, and government weather agencies.

Remote sensing is the process of detecting and monitoring the physical properties of an object from a distance. In atmospheric science, this refers to measuring reflected and emitted radiation of an area from the air, usually by aircraft or satellite (Stephens, 1994). Its roots go back to photographic images from balloons and aircraft. Applying remote sensing to observe weather from space gained traction in the 1950s and the first satellites with any weather sensing capability were launched in 1959. TIROS 1, launched in 1960, became the first dedicated weather satellite and 15 years later the first infrared imagery was processed (Vaughn, 1982; Kidder and Vonder Haar, 1995; Davis, 2007). Commonly referred to as imagery, these data are created from radiometers, not cameras. Radiometers are used to measure radiances, or the amount of radiation emitted and reflected from the Earth's surface, clouds, and atmosphere in a selected portion of the electromagnetic spectrum. Most measurements are done in the visible, infrared (IR), or microwave spectrum. Radiometers scan the view area line by line and measure the radiance of a specific area. Using

black body principles, radiances are then converted into brightness temperatures for interpolation into visual imagery for the forecaster (Hopkins, 2004). Since these first images, there has been exponential improvement in the temporal, spatial, and spectral resolution of imagers. In 1973, the DMSP was declassified, and it became public knowledge that the United States military had been utilizing a nighttime "visible" imager in the 1960s known as the Operational Linescan System (OLS) for intelligence gathering and weather monitoring (Lee et al., 2006; Liang et al., 2014; Seaman and Miller, 2015). This is the same system that saved Apollo 11. Since the original OLS, nighttime detection of clouds has greatly improved with the evolution of the Visible Infrared Imaging Radiometer Suite (VIIRS) Day/Night Band (DNB) which takes advantage of both visible and short-wave infrared (SWIR) wavelengths. Enhanced characterization of night-time cloud features is critical to improving many important forecasting problems on a variety of time and spatial scales (Miller et al., 2013).

During the late 1990's, a series of Cooperative Program for Operational Meteorology, Education, and Training (COMET) satellite meteorology courses were held, and the need for digital imagery that brings out features important to forecast weather warnings and forecaster duties was a recurring theme from participants. This led to the evolution of short-wave albedo and day/night albedo products (Kidder et al., 2000). These products revolutionized forecasting at the time but with new sensor capabilities and processing methods, imagery can still be improved upon.

1.2 Objectives and Outline of Dissertation

This project aims to create, quantitatively validate, and implement a multispectral imagery product for both polar and geostationary satellites that behaves as a pseudo-low-light visible sensor and can be quantitatively assessed. Specifically, the generation of these products will be used to monitor and gain a greater understanding of the nocturnal state of the atmosphere in efforts to improve low-cloud detection. This dissertation is organized into two main parts, the creation and validation of the machine learning (ML) nighttime visible imagery (NVI) for both polar and geostationary uses, and in-depth case studies demonstrating benefits gained from its application.

Chapter 2 provides background on radiative transfer theory which is key for the creation and validation of the JPSS NVI. Utilizing a feed-forward neural network (FNN), infrared channels from the VIIRS moderate resolution bands (M-bands) are combined and used to predict lunar reflectance created from the DNB. This demonstrates that while IR is thermal, and the DNB is a combination of reflective and thermal wavelengths, significant relationships in the spectral response functions at various wavelengths and wavelength differences can be capitalized on to simulate imagery made from lunar reflectance. The end result is a model that provides lunar reflectance values derived from infrared that is both qualitatively and quantitatively assessed against DNB lunar reflectance, proving the first quantitative assessment of nighttime visible imagery products to DNB measurements.

In Chapter 3, the JPSS VIIRS machine learning model is applied to the GOES ABI sensor suite to enhance spatial and temporal resolution. This combination of spatial coverage and temporal resolution is especially critical for short-term weather forecasters at low to mid-latitudes who rely on satellite imagery and cannot depend on the high resolution of polar orbiter imagery due to its infrequent revisit time outside of the polar regions. It addresses concerns in satellite intercalibration and provides support for wavelength substitution selection. Lunar reflectance values derived from GOES ABI input are again both qualitatively and quantitatively evaluated.

Chapter 4 highlights the many uses of the NVI for VIIRS and GOES satellites and focuses on case studies specific to our second goal, assessing coastal fog formation and applying the NVI to tropical cyclone forecasting challenges. In this chapter we provide examples to substantiate claims that this product can add value to these challenges that are lacking in current satellite measurements and derived products. Dissertation research and contributions to the field are summarized and future research recommendations provided at the end of Chapter 4.

Chapter 2

Turning Night Into Day: The Creation and Validation of Synthetic Night-time Visible Imagery Using the Joint Polar Satellite System (JPSS) Day/Night Band (DNB) and Machine Learning[1]

2.1 Introduction

Since its inception, satellite imagery has proved an invaluable resource for operational weather forecasters and atmospheric science researchers, critical in areas with limited surface observations such as coastal regions or open oceans. Forecasters obtain timely and actionable global atmospheric data for predicting hazardous weather conditions through satellites. Forecasters can look at cloud and moisture patterns at various wavelengths to discern weather phenomena of varying size and time scales such as frontal features, severe convection, fog, and cyclone life cycles. Visible imagery is the most easily interpreted type of satellite product as it allows for clouds to appear to the human eye how they would from the ground, but from space, which makes it more intuitive and ideal for real-time forecasters (Kidder et al., 2000). At night, forecasters must rely on IR imagery and methods for cloud detection which can make low cloud detection especially difficult due to the small thermal contrasts between the earth and low clouds at IR wavelengths.

There are several techniques used for cloud detection from imagers including threshold, histogram, pattern recognition, multispectral, spatial coherence, radiative transfer, and geometric techniques, each with its benefits and limitations. Cloud detection in the electromagnetic spectrum comes from satellite radiometers measuring emitted radiation at various wavelengths and is

[1]The results outlined in Chapter 2 have been submitted to *Artificial Intelligence for the Earth Systems*: (Pasillas et al., 2023)

based in radiative transfer theory. A perfect blackbody is one that absorbs all radiation, and in turn, emits all energy at a rate determined by its temperature. The specific spectral radiance of a blackbody for a given temperature is computed using Planck's Radiation Law. The Stefan-Boltzmann Law shows that the total radiance of an object is proportional to its temperature to the fourth power (Kidder and Vonder Haar, 1995).

Satellite detected radiances are converted to brightness temperatures for evaluation using knowledge of the spectral width and the Plank function as follows:

$$T_b = \frac{hc}{k\lambda} \ln^{-1} \left(1 + \frac{2hc^2}{I_\lambda \lambda^5} \right)$$

where T_b is the brightness temperature; λ is the wavelength, h is Planck's constant; c is the speed of light, I_λ is the measured intensity or spectra radiance at that wavelength, and κ is the Boltzmann constant. When emissivity is 1, the brightness temperature is equivalent to the thermal temperature of the emitting atmosphere. When clouds are present, this emitting temperature is generally colder. However, issues arise in this single-channel test when there are low clouds, thin clouds whose emissivity may be less than 1, or an inversion is present due to the low thermal contrast in these scenarios (Kidder and Vonder Haar, 1995; Liou, 2002; Chapman and Gasparovic, 2022).

Liou (2002) outlines the observed brightness temperature (BT) of a cloud-free atmosphere based on the absorption and emission of constituents in the atmosphere as seen in Figure 2.1. The two IR atmospheric windows are from 3-5 μm and 8-13 μm where absorption is fairly low. In this range absorption is continuous and the primary influence on spectral response is water vapor so measured radiance transmissions are solely of that surface and some water vapor unless there are intervening clouds (Liou, 2002; Petty, 2006). This makes these wavelengths an excellent choice for monitoring the atmosphere and many central wavelengths for sensors lie in this range because of this. It is important to note that there are differences in transmittance and associated brightness temperatures at the various wavelengths due to variation in atmospheric profiles from winter to summer and by latitude which can make it difficult to make one assumption valid for

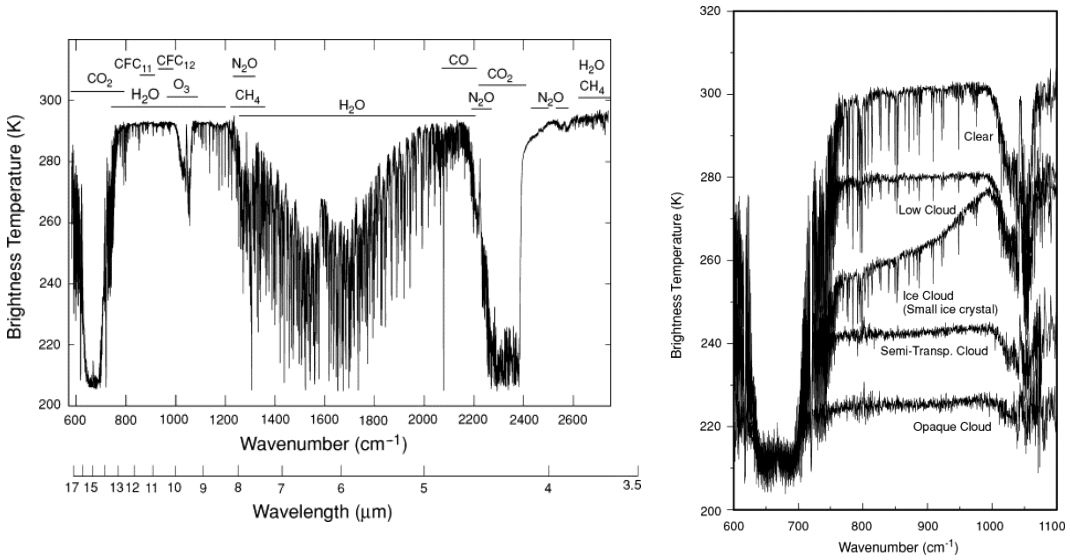

Figure 2.1: Observed infrared spectrum and absorption gases by spectral location from a high-resolution interferometer sounder (L) and brightness temperature spectra from a high-resolution infrared spectrometer indicating wavelength-dependent brightness temperature changes by cloud type (R). Figure taken directly from Liou (2002) 4.3 and 4.12.

global forecasting as at some wavelengths the difference in transmittance between a tropical region and subarctic winter can be over 60% (Chapman and Gasparovic, 2022).

Similarly, different cloud types respond in the wavelengths resulting in different brightness temperatures as a result of their particle size, composition, and optical depth (Stephens, 1994). One example of how different clouds respond, and anticipated brightness temperatures is in Figure 2.1. Generally speaking, in the IR, the colder the BT the greater chance there is cloud present, although very cold surfaces can also show up as cold BT. The warmer the BT the higher chance the scene is clear, or the clouds are low. From 10.2 μm - 14.3 μm the ice cloud signature has a strong slope, while the slope of the signature for all other conditions is minimal, thus calculating

BTs in this band region can aid in distinguishing between ice and water clouds since there will be a large brightness temperature difference (BTD) between wavelengths if ice is present.

This study will incorporate threshold and multispectral cloud detection techniques in the short-wave IR (SWIR) and long-wave IR (LWIR). In the threshold technique a BT at a specific wavelength is usually set to delineate whether a pixel is clear or cloudy. Creating a single cut-off temperature per wavelength creates issues when observing from satellites as the pixel value is an average of the scene below it and may not be representative of features smaller than indicated by the pixel resolution. Because of this, if a single wavelength is used, there are often two separate thresholds specifically to represent high confidence of clear and cloudy, with values in the middle of these two thresholds being undetermined or of mixed scenes (Kidder and Vonder Haar, 1995).

At the pixel level, multispectral techniques prove to be the most useful if only one technique can be used, as they account for the property differences of clouds at different wavelengths. Most cloud detection schemes are either focused on cirrus/high cloud or fog and low cloud and all can provide useful information to the overall environmental conditions especially if there are layered clouds. Near-surface clouds have similar BTs at infrared wavelengths as the Earth's surface beneath making it difficult to detect these clouds (Ellrod, 1995). While different wavelengths reveal important information on the atmosphere, it is the differences between wavelengths that highlight low-level cloud features best (Calvert and Pavolonis, 2010). Cloud spectral properties can be capitalized on through the use of not just the BTs of the various channels but also the BT differences (BTDs) when creating a new cloud detection product. Many previous studies have shown the benefits of using BTD for cloud property determination. Common techniques include the bi-spectral or split window technique (SWT), a comparison of the split window channel BTDs to surface temperatures, and tri-spectral comparisons for use with LWIR.

Low-cloud split window approaches typically use the 3.9 μm and 10.7 μm - 11.2 μm channels (Ellrod, 1995; Bendix, 2002; Hillger, 2008; Calvert and Pavolonis, 2010; Miller et al., 2022). Techniques with these wavelengths capitalize on the difference in spectral response functions previously shown at the two wavelengths as well as the fact that the 3.9 μm is a combination of

reflected and emitted radiation. Also known as the Nighttime Low Cloud Test (NLCT), this BTD set is one of the most commonly used tests for low cloud detection at night. The short-wave albedo or "fog product" of the 1990s GOES satellites revolutionized "fog and liquid water cloud detection at night" (Kidder et al., 2000). From this, Ellrod (2002) created a low cloud base (LCB) product for Instrument Flight Rules (IFR) conditions using the BTDs between 3.9 μm and 10.7 μm combined with surface temperature differencing. Studies demonstrated that when this BTD was less than 4K fog, or ceilings less than 1000ft, existed and when the BTD was between 4K and 6K a transition zone to IFR conditions could exist. The LCB product proved beneficial for aviation forecasters to identify fog formation. Because of this, we include BTDs that align with this range.

Inoue (1989) developed a cloud classification process using a combination of two threshold values in the 10.8 μm and two thresholds in the 10.8 μm - 12 μm BTD. This BTD can be near zero for clear skies as well as thin, moderate, and thick cirrus conditions but when combined with a -20C threshold and clear sky temperature threshold in the 10.8 μm, the result is a matrix for cloud detection categories of cumulonimbus, fog, thin cirrus, thick cirrus, and clear skies. This demonstrated that combining single wavelength temperature thresholds and BTDs leads to better performance than threshold or multispectral differencing techniques alone.

Infrared tri-spectral techniques were also used with the 8- μm, 11- μm, and 12- μm spectral regions (Strabala et al., 1994). Positive 8 μm - 11 μm BDTs demonstrate there is not a clear path in the atmosphere and therefore indicate clouds are present due to the aforementioned relationships in the EM spectrum. The 11 μm - 12 μm BTD is useful for determining cloud phase since the water response is effectively the same in these two wavelengths, but ice is more absorptive in the 12 μm vs the 11 μm, as seen in Figure 2.1, so large BTD values can indicate that there is ice present while the BTD is near zero for a liquid path. Combining these two differences in a scatter plot, Strabala et al. (1994) were able to determine if there was cloud present and its phase (helping to indicate cloud height and type) based on where on the slope it lies. Since VIIRS has all three bands both differences are included in the machine learning algorithm.

Several channel differencing products for cloud detection exist, but the visual results are often scaled images using color to represent features versus displaying what the features would look like to the human eye. This requires more forecaster training as each enhancement has its own mask color meanings (Chirokova et al., 2018). Because of this, we look to develop a nighttime imagery product that can be used across multiple cloud features, regions, and seasons without further manipulation. This imagery has clouds appear brighter than clear skies and land as they do in visible imagery making it more intuitive to the forecaster.

The DNB sensor enables radiance collection from 500nm to 900nm and can capture more detailed cloud features at night than LWIR (Min et al., 2017; Miller et al., 2013). The DNB sensor is currently only available on polar orbiters thus limiting its benefits to phenomena that do not evolve rapidly or that need only occasional snapshots. It is very sensitive to low levels of light and uses a 3-step gain system to detect radiances over eight orders of magnitude, utilizing lunar illumination and even air glow as its light source for nighttime imagery and full sun for daytime solar illumination (Miller et al., 2013; Liang et al., 2014; Seaman and Miller, 2015; Seaman et al., 2015; Zinke, 2017; Line et al., 2018). Normalizing this range for visual presentation is often challenging and all DNB radiances must be scaled post-processing to create imagery usable by the human eye (Zinke, 2017).

There are many DNB scaling schemes available for forecasters depending on what phenomena they are trying to detect, the phase of the moon, and presence of other ambient light sources. Each scaling has strengths and weaknesses, and some require external resources beyond the VIIRS sensor data records (SDRs), which can make utilization more difficult for the end user. The most common scaling is the near constant contrast (NCC) which makes all imagery in the scenes appears to have uniform illumination regardless of the lunar or solar influences and has its own VIIRS Environmental Data Record (EDR) (Liang et al., 2014; Seaman and Miller, 2015; Zinke, 2017). The NCC reduces the radiance dynamic range to three orders of magnitude creating a pseudo-albedo. A limiting factor of the NCC is that adjustments to account for lunar phase and user

preferences can cause values to be visually displayed quite differently from user to user (Seaman and Miller, 2015; Zinke, 2017).

Another useful scaling is the 'erf-dynamic scaling' (EDS) by Seaman and Miller (2015). This scaling algorithm depends solely on the DNB SDR and utilizes the Gauss error function to relate anticipated maximum and minimum radiance values to the image gray-scale to provide useful imagery under all-natural lighting conditions regardless of the lunar cycle. The high and near constant contrast (HNCC) created by Zinke (2017) attempts to create a single scaling that works for all phases of illumination and is independent of look-up tables like the EDS. Similarly, the HNCC utilizes a normalized radiance value instead of a pseudo-albedo but retains solar and lunar zenith angle-dependent gain functions like the NCC. In all of these methods, which are available in some capacity regardless of the lunar cycle, users rely on post-processed imagery, which limits them to a qualitative validation with visual inspections or comparisons (Line et al., 2018).

The spectral irradiance and radiance of the moon have been under observation by NASA since 1996 and lunar radiometric models from this data are used to calibrate on board sensors of satellites (Kieffer and Stone, 2005). Miller and Turner (2009) published a dynamic lunar spectral irradiance data set and model with look-up tables for top-of-atmosphere (TOA) radiance and irradiance. These expedited calculations of irradiance, making it possible to calculate a lunar reflectance value (between 0-1) for all measured DNB radiances and enables quantitative studies of the DNB to assist in conducting comparison calculations as is done with the data in the visible spectrum. Imagery from these calculations are typically limited to just over half the lunar cycle due to moon angle and phase. Min et al. (2017) evaluated the potential changes of nighttime reflectance from these irradiances and determined that nighttime reflectance differences are less than .05% for water clouds between lunar phase angles demonstrating that a DNB-based nighttime cloud retrieval will have minimal impacts quantitatively due to the lunar phase, though visually it may present vastly different.

The concept of nighttime visible imagery has gained significant popularity since the launch of JPSS with the DNB and a number of techniques have been developed in recent years to create syn-

thetic "nighttime" visible imagery from IR channels available on other satellites (Chirokova et al., 2018; Kim et al., 2019, 2020; Kim and Hong, 2019; Mohandoss et al., 2020; Harder et al., 2020). Most methods use machine learning to create a "nighttime" visible imagery and exploit relationships seen in the wavelengths with daytime visible imagery, though one product used regression and the DNB sensor.

Harder et al. (2020) present results of three different U-Net based models from a Hackathon in which they used ABI channels 1-6 as target visible red, green, blue (RGB) imagery composites and ABI channels 8-16 as the predictors. They present a visual comparison of the models to each other and RGB composites for day and nighttime and use SSIM and RMSE for quantitative assessments. Their best performing model was a UNet ++ and had a SSIM of 0.86 and RMSE of 0.07 but results are, of course, very sensitive to the scenes being analyzed (Harder et al., 2020). Many attempts have been made to create nighttime visible imagery with generative adversarial networks (GANs) and Conditional GANs (CGANs) (Chirokova et al., 2018; Kim et al., 2019, 2020; Kim and Hong, 2019; Mohandoss et al., 2020; Harder et al., 2020). Evaluation of these models had been predominately through SSIM, RMSE, MAE, and CCs in comparison to daytime visible images with varying results. CIRA's proxy-visible imagery uses scaled VIIRS DNB radiances as truth and multiple linear regression to create a product that combines 3.9 μm with LWIR channels. Proxy-visible is used operationally by the National Hurricane Center to aid in tropical storm tracking at night (Chirokova et al., 2018). Qualitative comparisons for nighttime imagery have been to either IR channels or to "no observation" since there is not nighttime imagery available on geostationary satellites. Quantitative assessments on nighttime visible imagery are challenging given the qualitative nature of most image products, and details of the scenes used for assessments.

The aforementioned techniques demonstrate improvement over the use of IR only and work to close the latency gap and lunar inconsistencies in scaled DNB imagery, however, there are still great strides to be made in the field of cloud detection via remote sensing. We propose to use machine learning methods and LWIR to create a nighttime imagery product, Machine Learning Nighttime Visible Imagery, or ML-NVI. The ML-NVI is a pseudo nighttime visible imagery prod-

uct derived from LWIR and validated using the DNB sensor. Unlike previous methods, it computes a physically based albedo that can be compared quantitatively to the DNB albedo. The albedo is then used to create imagery that capitalizes on forecaster intuition. It is not an exact translation of all clouds but rather visually accentuates low and layered clouds to the user and performs well in overall detection of clouds. Created and validated initially using JPSS channels, its input channels were selected to be transformable to the GOES ABI sensors to gain temporal and spatial resolution. It is trained and validated on the Miller and Turner DNB lunar reflectance therefore a quantitative, not just qualitative, nighttime assessment is able to be completed and set as a new standard metric across the field.

The remainder of this chapter delves into the development, testing and validation of the ML-NVI. Section 2 highlights data selection and processing. Section 3 focuses on the model architecture selection and training processes resulting in a preferred scheme. Section 4 provides the general validation of ML-NVI while Section 5 is the summary and conclusion.

2.2 Data

We used JPSS NOAA-20 and SNPP data over the open northern Pacific Ocean from December 2018 – November 2020 corresponding to the occurrences of a full moon +/- 1 day to create the base data set for training, validating, and testing our model. Both the NOAA-20 and SNPP are equipped with the VIIRS. While Lin and Cao (2019) demonstrated that their relative spectral responses (RSR) are not identical differing between 0.18K- 0.06K, we assumed this minimal difference in sensors as in reasonable performance limits and included data from VIIRS off both systems when creating the training data set and do not adjust for seasonal variations to train a model that results in a single product that is valid for all seasons and both satellites.

This created 25 sets of 90+ matching date-time groups (DTGs) that could be divided by meteorological season or latitude if desired. The open ocean area of interest (AOI), seen in Figure 2.2, extends from 0N to 50N and from 180W to 127W. This AOI was chosen to minimize complications from city lights and vegetation differences over land and account for various background

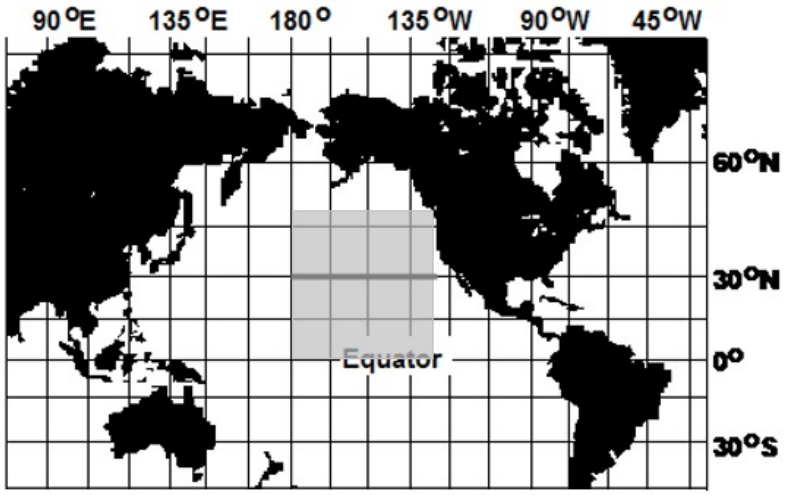

Figure 2.2: Area of Interest (AOI) for the study was a bounding box 50N, 0N, 125W, 180W. AOI was further divided into two subregions at 30N. Base map modified from https://web.ics. purdue.edu/ braile/edumod/epiplot/epiplot.htm

sea surface temperatures (SSTs) which range on average between 5C to 30C in this region over the course of the year. The total region (0N-50N) was further divided into two subsets by latitude range (0N-30N, 30N-50N) as well. This created three latitudinal models in order to evaluate the differences in training and validation over tropical versus mid-latitude SSTs, atmospheric profiles, and cloud features. It is possible that equivalent channel BTs in two regions may be tied to significantly different features: in one region it may be clear skies, but in another it may be upper-level cirrus or low-lying uniform fog. The division in training and assessment by latitude is to help differentiate between the scenes and potentially calculate values for clear scenes more readily. Accurate clear scene temperatures are critical in any assessment of clouds as the clouds are the deviations from the anticipated radiation (Stephens, 1994). This latitude division also aimed to evaluate how much benefit there would be, if any, for latitude-trained specific models versus a global use model.

Training and testing data were from December 2018 - November 2019 and the models were validated using December 2019 - November 2020. An additional data set spanning May 21, 2020 – July 20, 2020 was used to qualitatively assess the contrast consistency of ML-NVI imagery across the full lunar cycle. To reduce any bias from view angles or the bow-tie effect, training and

validation data sets were adjusted to only include data in the first aggregated scan of the DNB, specifically to only include 600 pixels to the left and right of nadir. The final input set for training data consisted of an array sized 1947x512x512x10 representing the number of images per scene, data set dimensions in the x-y plane, and the number of predictors for data in the prescribed AOI. The VIIRS validation set consisted of 2074 patches 512x512x10 predictors (channels) deep. These patches enabled the ability to visually plot the data for quantitative comparisons but were flattened to approximately to arrays with dimension 510,394,368 X 10 and 543,686,656 X 10 respectively for training and statistical calculations as these were done at the pixel level. All data for this research is available on the National Oceanic and Atmospheric (NOAA) Comprehensive Large Array-data Stewardship System (CLASS) server (https://www.class.noaa.gov/).

Table 2.1: List of Predictors used in the VIIRS ML-NVI creation, associated central wavelengths or wavelength differences, wavelength range, and associated prior research applications.

VIIRS Band	Central Wavelength or Brightness Temperature Difference	Wavelength range	Prior Research Use
M13	4.05	3.97 - 4.13	
M14	8.55	8.4 - 8.7	
M15	10.763	10.26 - 11.26	
M16	12.01	11.54 - 12.49	
M13M14 BTD	4.05 - 8.55	*	
M13M15 BTD	4.05 - 10.763	*	3.9 and 10.35 Legacy fog product (Ellrod 1995, Ellrod and Gultepe 2007) Wetzel et al 1996, Bendix 2002, Hillger 2008, Miller et al 2022 3.75 and 10.8 (Kim and Hong 2019)
M13M16 BTD	4.05 - 12.01	*	3.75 and 12 (Kim and Hong 2019, Anthis and Cracknell 1999)
M14M15 BTD	8.55 - 10.776	*	8- -11- (Strabala and Ackerman 1994)
M14M16 BTD	8.55 - 12.01	*	
M15M16 BTD	10.763 - 12.01	*	10.3 and 12.3 (Prabhakara et al 1974, McMillin 1975, Inoue 1989, Strabala and Ackerman 1994, Stephens 1994, Lindsey et al 2014)

The model predictors and associated wavelengths can be seen in Table 2.1. Initial channel selection was based on wavelengths with similar bands between the VIIRS and ABI sensors and was limited to the M-bands for resolution consistency. The BTDs selected were based on wavelengths relationships highlighted in the literature review. Considerations for channel combinations

included all four of Hillger's recommendations for satellite product development (Hillger, 2008). Band normalization was done to the sensor capabilities for each band as seen in the VIIRS Algorithm Theoretical Basis Document (ATBD).

To best create and validate the ML-NVI model, the resulting predictand must be able to be qualitatively and quantitatively compared to a truth. The only nighttime visible data comes from the DNB radiances. DNB radiances must be scaled or modified for use with the human eye and there is no single standard scaling scheme. While scaling of radiances makes visually appealing imagery to the end user there is no way to quantitatively compare different procedures unless the same scaling is applied throughout, thus scaled imagery values are not the preferred truth as the validation would be an assessment of recreating a specific scaling not against a measurable quantity. Lunar reflectance was selected as the truth data for our study since it is a direct manipulation of measured DNB radiances and enables direct quantitative comparisons to nighttime data from satellite retrievals. This allows for a quantitative evaluation of the ML-NVI itself that has previously been described only for daytime visible imagery or nighttime IR.

2.3 Model Architecture and Training

We trained a Fully Connected Neural Network (FNN) model to create the ML-NVI from IR BT and BTDs. The FNN accounts for non-linearity and processes data pixel by pixel which enables us to further restrict the training data set more easily if needed. Input to a FNN can be of any dimension, but for the purpose of this model, we chose our inputs to retain a multiple of eight in x-y dimensions for ease to translate the training data sets to other machine learning architectures if necessary. As seen in Figure 2.3, the final baseline FNN model has ten inputs and is composed of three hidden layers (the first two with eight and one with four nodes) using Rectified Linear Unit (ReLU) activation and a single node for an output layer that uses sigmoid activation. The model uses an Adam optimizer value of .001 and mean square error (MSE) for its loss function. The number of hidden layers and nodes were chosen after sample runs indicated there was no

significant increase to the learning done with further increase in the number of hidden layers or nodes.

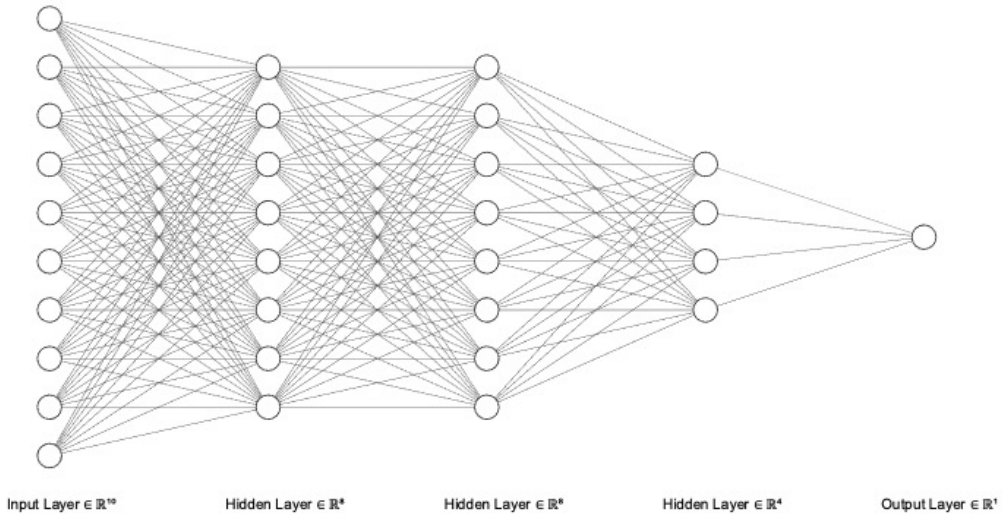

Figure 2.3: AI Architecture for the ML-NVI. ML Architecture consists of 10 inputs, 2 hidden layers with 8 nodes, 1 hidden layer with 4 nodes; all with an Adam optimizer, MSE loss function, and RelU activation functions; and a single node output layer using the Sigmoid activation function. Training data was then processed through the model for 40 Epochs with a batch size of 2048.

Training data was then processed with this base model repeatedly over various batch sizes and epochs for the three latitude ranges of interest. Results of this can be seen in Table 2.2. It was noted that regardless of batch size and latitude data input, training tended to level off after 5-10 epochs and then again around 20-30 epochs, though the value gained by these extra epochs was minimal in comparison to the values gained in batch size trade-offs. The metric results between varying the batch sizes between 256, 512, 1024, 2048, and 4096 demonstrated that the value gained from smaller batch sizes was minimal in relation to the additional training time. A final epoch size of 40 and batch size of 2048 was chosen to balance out training time and CPU memory with the benefits gained. Training data sets from each latitude range (0N-30N, 30N-50N, and 0N-50N) were processed to create three separate latitudinal models from the base architecture.

Table 2.2: Training iterations for the FNN used to determine the preferred model set- up. Models with 40 epochs and a batch size of 2048 performed the most consistently regardless of the latitude associated with the training or validation data.

MODEL: (epoch/batchsize)	TRAINING DATA LATITUDES	MODEL METRICS MSE	MAE	V-MSE	VMAE
10, 256	0N-50N	0.0175	0.0872	0.0179	0.0867
	30N-50N	0.0285	0.1212	0.0287	0.1223
30, 512	0N-50N	0.0204	0.0988	0.0203	0.098
	30N-50N	0.02828	0.1206	0.028	0.1202
	0N-30N	0.0083	0.065	0.00826	0.0605
30, 2048	0N-50N	0.0178	0.0884	0.0177	0.0884
	30N-50N	0.0289	0.1219	0.029	0.1251
	0N-30N	0.0086	0.062	0.0086	0.0625
40 ,2048	0N-50N	0.0174	0.0868	0.0175	0.087
	30N-50N	0.0294	0.125	0.029	0.125
	0N-30N	0.00847	0.0613	0.00848	0.0622
30, 4096	0N-50N	0.0197	0.094	0.0198	0.094

2.4 VIIRS Validation and Results

Loew et al. (2017) stated that "the ultimate goal of a validation exercise is to assess whether a data set is compliant with predefined benchmarks (requirements) that quantify whether a data set is suitable for a particular purpose." Kidder et al. (2000) elaborated on this point, highlighting that satellite-derived products and algorithms need to provide an accurate analysis of the important meteorological features and "do not need to work on the unimportant features of the image." As an example, he further explained that "an algorithm designed to monitor a low-level feature such as fog/stratus does not need to be precise for high cold clouds." The purpose of the ML-NVI is to detect clouds with a focus on low clouds that are otherwise difficult to detect at night, and present them as visible imagery. Considering this and the intent of the product, focus for ML-NVI imagery qualitative validation will be on low clouds at night while quantitative assessments were done for overall performance of lunar reflectance.

There are requirements for the accuracy of radiometers and required skill scores for various radiance derived products but there are currently no predefined benchmarks for imagery validation. The closest benchmark would be the imagery and validation efforts and analysis methods from NOAA-NASA for the ABI channels. This process first conducts visual inspection for feature determination and temporal image consistency, then a qualitative comparison with imagery between legacy and current GOES as well as polar orbiters is done to assure at least similar quality. Afterwards, a quantitative comparison of reflectance and brightness values from level 1b radiances and ground calculated values is used Pitts and Seybold (2010).

Similar to Pitts and Seybold (2010), we first conduct qualitative analysis between DNB lunar reflectance, the three latitude ML-NVI models, and two VIIRS M-band IR channels (M13 (4.05 μm) and M16 (12.01 μm) at the full moon. These comparisons can be seen in Figure 2.4. The scenes from top to bottom comprise three sets of two samples for general cloud and special feature detection (row 1 and 2), fog (row 3 and 4), and tropical cyclones (row 5 and 6). Thin cirrus (present in many samples) appears bright white in the IR and blocks the underlying clouds, but in the three models appears as a semi-transparent mask that you can "see through" to the clouds beneath and is often not present in the DNB. Due to its transparency, we can still detect low to mid-clouds in layers below it that are absent or blocked in the IR imagery. Additionally, all latitude models capture low-level clouds, such as open ocean stratocumulus, that are visible in the DNB lunar reflectance but not captured well, if at all, in the IR samples as seen in Figure 2.4, rows 2, 4, though the contrast is best in the full-latitude model. Though not as bright as DNB lunar reflectance, it is possible to infer the layers clouds in the models just like the DNB with higher/thicker clouds being brighter (colder) in comparison to lower clouds and with more contrast for lower-level features than seen in the IR. In comparison to the single-channel IR wavelength imagery, the human eye can more readily pick up the low-level cloud features in the models and background scene differences between land and water more readily when land is present. As model predictions are created from thermal emissions, its contrast between clear skies and clouds do not appear as vividly as the true DNB lunar reflectance but the clouds appear brighter than the clear areas and intuition would show a

human forecaster that low and layered clouds are present in the scene that would be missed by IR interpretation alone.

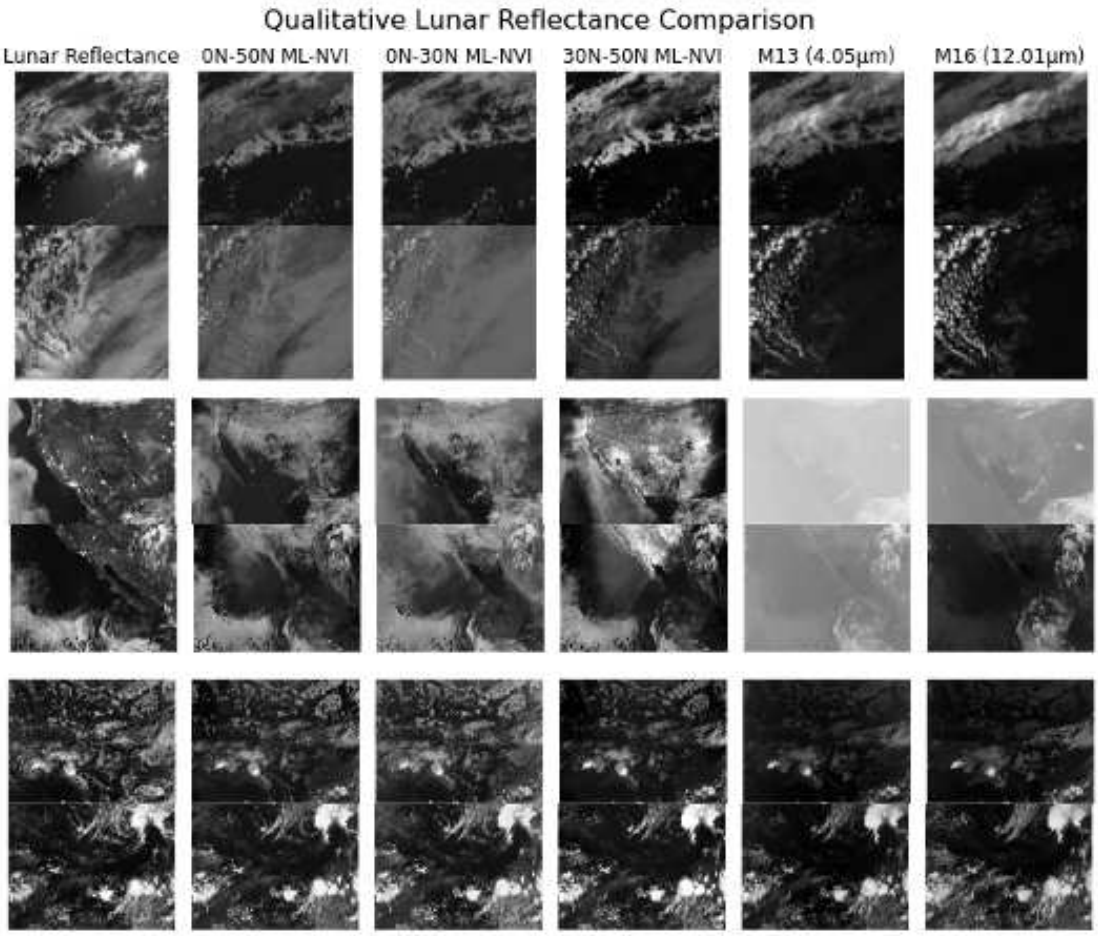

Figure 2.4: Qualitative Comparisons (Left to Right) of images from DNB radiance calculated lunar reflectance, predicted lunar reflectance for the three latitudinal models (Full-latitude, Low-latitude, Mid-latitude), and VIIRS M13 (4.05 µm) and M16 (12.01 µm) sensors. The top two rows highlight general cloud features, the middle two rows are fog events, and the bottom two rows are a tropical storm event.

The NVI highlights the fog better than the IR and is helpful for detecting the fog extent when not possible with DNB due to illumination. Fog events are present in Figure 2.4, rows 3 and 4. Comparing the model imagery to the DNB, all models captured fog when it was over warmer waters such as south of Mexico although the 30N-50N model over predicts it (row 4) but only the full-latitude model captured fog well over colder SSTs (row 3). When comparing the ML-NVI to the IR, especially noticeable is how clear the extent of fog appears and the texture in the ML-NVI.

We also see the location of the California coastal current compared to the open ocean in the ML-NVIs due to the significant temperature SST contrast; however, its uniform smooth texture helps to identify it as such versus low clouds for visual analysis.

A tropical storm is present in Figure 2.4, rows 5-6. The low-level circulation and texture of clouds remain apparent in both the DNB and model imagery but are lacking in the IR imagery. This demonstrates that we can use ML-NVI to find low-level closed circulations (LLCCs) at a better skill than with IR alone and when DNB is not available.

The models also address artifacts that appear in DNB lunar reflectance; specifically, the models remove lunar glint (Figure 2.4 row 1) as well as man-made lights (Figure 2.4 rows 3 and 4). In the absence of city lights, populated areas appear darker (warmer) than the surrounding land which may be capturing the presence of urban heat islands. While the focus of the models is for use in ocean and coastal regions, these samples demonstrate performance over land. Though the appearance and contrast vary, all models are able to capture ship tracks and aircraft contrails, and provide better texture of clouds to help indicate actual cloud features versus a uniform field as seen in IR.

Each latitude model addresses cloud types differently because the models were only trained on data (SSTs and cloud types) specific to that region. The impact of latitude-specific trained models and their use for other regions is most apparent in Figure 2.4 rows 3 and 4. The model trained on data from 0N-30N has the least contrast of the three models over these samples. This is because the observed BTs in the predictors are much colder than the tropical SSTs that represented clear skies so the model assumes that there must be inference to the surface and the BT interpretation is a reflectance indicative of a constant thin cloud layer over cold SSTs. This model did have decent contrast and performance in the TC examples and scenes over warm SSTs. This demonstrates that this model will only perform well with warm background SSTs. The model trained from 30N-50N appears to have the greatest contrast of the three models and may be the closest to the DNB at first glance in rows 1,2. It performs similarly for the TC samples though more washed out than the low-latitude model. Its shortfalls are most noticeable in the fog samples where it does not perform

well for fog identification and has a distracting contrast over land masses. Qualitatively, the full-latitude model performed best for all the cloud types and accounts for all SSTs between 0N-50N that are seen in open oceans, appearing similar to the low-latitude model in the tropics and to the mid-latitude model in the middle latitudes.

Comparisons of the distribution of the three latitude model predictions for the validation sets relative to each other and the true reflectance can be seen in Figure 2.5. Note that the lunar reflectance value distribution is not normally distributed. The probability density functions (PDF)s further highlight not only the percent of observations types (i.e. reflectance values) but also visually demonstrates differences in cloud detection ability at various reflectance values. Areas of low reflectance, indicative of clear skies (and the majority of the data), were well matched throughout all three models, though visually we see how the differences appear when turned into imagery. The middle reflectance values are the hardest to detect and may be indicative of layered clouds, low or mid-level clouds, or scenes where the cloud features are smaller than satellite pixels. The full-latitude model appears to perform best in these cases. The highest reflectances represent optically thick clouds and thunderstorm clouds that are typically well identified in the IR due to the strong thermal contrast. Cursory looks of the PDFs indicate that the full-latitude model has the highest agreement to the truth across the reflectance spectrum.

Based on qualitative analysis and model prediction distributions, the full-latitude model (0N-50N) appears to be the best-performing model for mid-latitudes (followed by the 30N-50N model and the 0N-30N model) and it is very similar in model performance to the low-latitude model for performance in the tropics with the mid-latitude model being the worst. The full-latitude model reflectance values are the most closely aligned to the DNB reflectance and provided the best representation of clouds among the three models with minimal loss of information. Because of this, the full-latitude model is the model of choice, and the remainder of model validation will be on the full-latitude model, hereby referred to as the ML-NVI.

Figure 2.6 shows comparisons for select scenes that highlights various phenomena forecasters may be interested in. From left to right are lunar reflectances calculated from the measured DNB

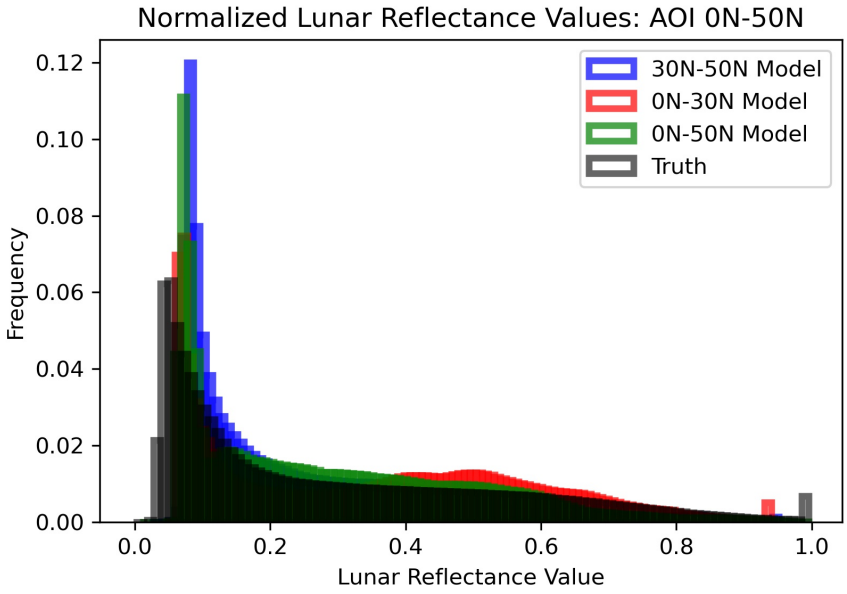

Figure 2.5: Probability Density Functions of the three latitudinal model lunar reflectance distributions versus the true DNB lunar reflectance distribution for the 0N-50N validation AOI.

radiances, predicted lunar reflectances from the full latitude model, visual depictions of the value differencing between the truth and model, and IR imagery at 12.01 μm which helps to highlight the features captured that may lead to greater changes between the truth and prediction. Negative (positive) differences in the two measurements seen in red (blue) indicate pixels where the model depicts higher (lower) lunar reflectance values than the DNB lunar reflectance. Looking at the different examples, this is most commonly seen when the model lunar reflectance imagery is depicting upper-level cirrus that is not captured by the calculations from DNB radiances. This leads to a higher lunar reflectance value for the same region than what is captured by the DNB lunar reflectance. A difference is not inherently bad for areas of cloud cover but demonstrates that the model lunar reflectance captures more cloud and different cloud types than the DNB lunar reflectance when clouds are present, and forecasters need to be aware of this signature. This can be beneficial for forecasters looking to identify cloud-free line-of-sight vs obstructed line-of-sight. The minimal difference values and contrast in the third image of row two highlights that the model handles clear skies well when there is a true cloud free line of site and no intervening cirrus. Low cloud that is missed in the IR and present in the DNB lunar reflectance is captured in the model

depiction though significant differences between the DNB and model lunar reflectance are seen by the larger positive (blue) differences for the convective activity. This may be due to the moon angle and moonlight highlighting vertical extent and texture creating a 3D feature in the true lunar reflectance that is not captured well by the model which instead smooths out the convective features. Row three demonstrates what can happen to the contrast in an overall scene when there is a large thin cirrus presence that is captured by IR but not captured by DNB. Without looking at the IR, one may think this is a poor representation of the DNB but in reality, it highlights all the cirrus present and identifies the low cloud below it. The fourth row demonstrates potential use of the model lunar reflectance for the identification of air and ship trails that are missed in both the DNB lunar reflectance and the IR. The final row demonstrates what can happen to land observations and shows strong differences in reflectance values of the Hawaiian Island chain.

In addition to analysis at full moon, a qualitative assessment was done on ML-NVI performance over the full lunar cycle for the model of choice. Figure 2.7 makes comparisons between the full latitude model imagery, DNB lunar reflectance, and the VIIRS M16 (12.01 μm) IR images for two lunar cycles at approximately one quarter moon intervals starting shortly before a full moon. During the majority of the lunar cycle lunar reflectance data is not available (as seen by the black images for lunar reflectance in rows 1,3-5, 8) and other DNB scaled products must be used. Since LWIR is fully emissive and the model was trained solely on full moon scenes, model reflectance values do not respond to the solar or lunar cycles and the ML-NVI provides lunar reflectance values and DNB like visual imagery with consistent shading across the lunar cycle. This allows users to learn only one presentation of features versus varying representations. In comparison to the IR, as before, the ML-NVI appears to capture most features and spatial patterns highlighting lower clouds and detecting layered clouds most apparent in rows 1,4, and 7. Additionally note the presence of the Big Island of Hawaii in the lower half of rows 2 - 4 and its presentation in the different data sets. ML-NVI can provide night-time visible imagery, even when DNB is not available, that enhances cloud identification over IR alone.

Next, statistical calculations were conducted to assess the overall capability of the ML-NVI for full moon scenes over open ocean. The product is designed to function regardless of moon phase, however, model creation and quantitative validation was conducted near the full moon, as this is when the highest quality DNB data is available for comparison. While the validation data also occurred at full moon, visual inspection determined there were periods where the moon was below the horizon for part of the scenes leading to a region of lunar reflectance equal to zero and black corners in the visual depiction of true lunar reflectance similar to when there is no moon. These points account for approximately 2% of the data and were removed before statistical calculations were performed. Reviewing the sample difference plots in Figure 2.6 data points over the Hawaiian Islands as well as scenes with moon-glint may have adverse impacts on the statistical calculations as these features were not removed during statistical calculations since there was not land or moon glint flags to identify and distinguish these pixels. Though only accounting for a small portion of the data, the inclusion of these features (Hawaiian Islands and moon glint scenes) may account for some of the spread and deviation in the quantitative evaluation of the model.

Validation is performed not only by evaluating the specific pair of observational points but also by evaluating the underlying PDF. In addition to the previously discussed PDFs in Figure 2.5, a scatter plot of the full latitude model's performance versus the true DNB lunar reflectance can be seen in Figure 2.8. The lower left corner represents clear skies with true and predicted lunar reflectance values of zero and the upper right represents full lunar reflectance values in each. The scatter plot shows a positive trend between the data sets. In some areas the data are more widely distributed along the one-to-one line but the relative differences in the data set are small. The difference between full-latitude predicted and observed lunar reflectance values are also plotted in Figure 2.8 with a mean difference of 0.43 and a standard deviation (SD) of 11.86. The Word Meteorological Organization (WMO) suggests that for cloud cover comparisons, data and models/predictions be divided into cloud categories though they do not specify thresholds (Zhongming et al., 2012). WMO height and total cloud cover categories for Observations and Terminal Aerodrome Forecasts usually line up with aviation flight safety requirements (Weiss, 2001). A review

of research shows that most studies divide the total cloud cover into observational categories based on sky octa obscuration (clear, few, broken, scattered, and overcast), into 3 categories (clear, partly cloudy, cloudy), or into 10% bins (Warren et al., 1988; Hogan et al., 2009; Zhongming et al., 2012). With this in mind, the reflectance values from our model demonstrate to be within a reasonable range difference and most differences would be only one category off in the most stringent 10% binning scenario.

Table 2.3: A consolidation of the validation metrics for the full-latitude model across all three validation regions. Scores for the full-latitude model in the 0N-50N AOI demonstrate model performance for use of a singular global model across all seasons.

2020 ML-NVI VIIRS VALIDATION METRICS									
MODEL	Validation Latitudes	Explained Variance	R2	RMSE	MAE	Spearman Coor	Corrcoef	KLD	JSD
0N-50N Full Latitude	HEMI	0.758	0.758	0.00	8.2	0.861	0.87	0.077	0.139
	MIDLAT	0.67	0.667	0.00	11.34	0.823	0.822	0.084	0.148
	TROPICS ALL	0.802	0.79	0.00	6.35	0.869	0.898	0.066	0.126

Quantitative scores for the model are for the overall data set and not calculated for or weighted based on the reflectance distribution. A chart of the statistical results for the full-latitude model assessment at the three validation latitudinal bands is provided in Table 2.3. There is currently no other published data utilizing lunar reflectance to provide baseline metrics for direct comparisons. As data becomes available it will be critical to ensure comparison metrics are made between similar data sets. The differences in explained variance (0.67-.80) corresponds to general cloud cover expected in the regions. The areas with the greatest variance explained by the model corresponds to regions with more clear skies while regions with more varied lunar reflectance values, indicative of increased clouds, have the lowest variance explained. This further highlights that while there are many useful relationships in the inputs used in our model, information on spatial context may improve skills in variance for clouds features even though spectral data can be a good indicator for cloud free regions. The ranges of MAE and RMSE further demonstrate the spread of the data and, like the standard deviation, are within a reasonable amount when considering that lunar reflectance is a visual proxy for total cloud cover. The Spearman's Correlation and correlation coefficients

between the ML-NVI and DNB true lunar reflectance range between 82% and 89% indicating a strong positive relationship between the two.

Additionally, to quantify this relationship, Jensen Shannon divergence (JSD) scores were calculated. JSD scores range between 0-1 with the lower number indicating the similarity or minimal divergence between the two sets. The JSD scores for the full latitude model ranged between 0.12 and 0.15 and indicate there would be only a small adverse impact if the ML-NVI values were to be used in place of the DNB lunar reflectance for modeling or calculations if using the full latitude model to create lunar reflectance (Loew et al., 2017) as demonstrated in Figure 2.7 with the full lunar cycle. This highlights the ability to have a greater visibly intuitive product with a scaled consistency for forecasters across the lunar cycle as the ML-NVI predicts what a full moon lunar reflectance would be regardless of the actual moon phase, angle and existing lunar reflectance and the ability to use one model (full-latitude) for the whole globe. It is possible to infer what lunar reflectance's would be expected for the observed phenomena at any lunar phase if a full moon existed instead based on the lunar reflectance values created from our model. From this it could be possible to even utilize daytime cloud mask algorithms at night if the day and night reflectance differences in the 3.9μm band are accounted for (Miller et al., 2022). ML-NVI improves upon currently used DNB scaling methods many of which use techniques dependent on the moon phase to make imagery appear constant across the day night terminators and for various moon phases.

2.5 Discussion and Conclusion

In this study a ML model to replicate lunar reflectance was created using IR and provides night-time imagery to the end user that behaves similar to DNB and solar visible imagery. Evaluations of the ML-NVI were conducted with scores as seen in Table 2.3. We have demonstrated both qualitatively and quantitatively the ability to turn night into day and create visually consistent night-time visible imagery from IR across the full lunar cycle.

ML-NVI can enhance the detection of low clouds at night over traditional IR, which is especially critical for coastal fog formation and tropical cyclone forecasting. Enabling a forecaster to

better visualize fog formation, extent, and dissipation can enhance flight safety and aid to minimize impacts from fog to busy coastal airports and for mariners at seaports. One of the key elements of forecasting fog dissipation is the point of the forecast location with respect to the fog boundary (Gurka, 1978b,a). The ML-NVI provides good ability to detect this boundary as seen in Figure 2.4. The 5th row is of a coastal fog event off of Mexico on October 6, 2017 when there was 99% illumination while the row below it is for an event on September 7, 2020 with 82% illumination. All three products can identify the fog, however its' extent and optical depth is much more apparent in the Lunar Reflectance and the ML-NVI over the IR alone. From this one may be able to determine more precisely the extent that the fog layer and time its dissipation.

The Operational Linescan System (OLS), the predecessor to the DNB, determined there was a 1-2 degree/ 60-120 nautical mile difference in pinpointing the center position location of tropical cyclones between using IR and nighttime visible sensors for low-level circulation. The turn to using nighttime visible sensors such as OLS and DNB over IR when available had significant effects on wind fields and forecast timing (Miller et al., 2006). By using the NVI in the same capacity as OLS or DNB, center position fixes may become more precise than current nighttime IR fixes as illustrated previously. Furthermore, animated ML-NVI imagery can help separate the layers of cloud rotation and improve tropical cyclone intensity using Dvorak techniques and structure knowledge in comparison to LWIR animations. Rows 7-10 in Figure 2.4 show image comparisons for Tropical Cyclone Lane from 20180825 1247z – 20180827 1304z. While a significant hurricane before this date, Hurricane Lane hit significant wind shear and quickly deteriorated. In the period displayed, Tropical Storm Lane went from a tropical storm to a tropical depression and strengthened to a tropical storm again despite its interactions with wind shear. Lunar Reflectance and NVI imagery highlight the lower-level closed circulation (predominately on the western half of the storm) better than the IR imagery for the same times throughout the series but especially when the storm was downgraded to a depression for August 26, 2018 as seen in Figure 2.4, rows 8 and 9.

The implications on environmental applications are numerous. First, the ML-NVI provides a product that improves the contrast issues across the day/night terminator seen in most DNB products and preserves a constant contrast regardless of the lunar cycle. This is more intuitive to a forecaster and does not require additional calculations or look up tables as may be needed for other DNB products that are made available throughout the lunar cycle. The ML-NVI can be done at near real time at processing centers such as CIRA for distributed use versus requiring end users to do further manipulation at their workstation, giving greater accessibility to the product. Next as seen above, NVI can enhance the ability to detect fog and low-level tropical circulations more easily that IR alone. It also projects layered clouds in a more transparent manner to a single image as seen by its representation of both the thin upper-level cirrus and low-level clouds. The secondhand impacts to aviation safety are vast. These examples demonstrate the use of NVI and benefits it can bring on the JPSS systems. When NVI is further translated into ABI sensors, persistent nighttime imagery will be possible via the GOES satellites for enhanced tropical cyclone tracking and positioning and more precise timing of fog formation and dissipation and visualization of coverage extent.

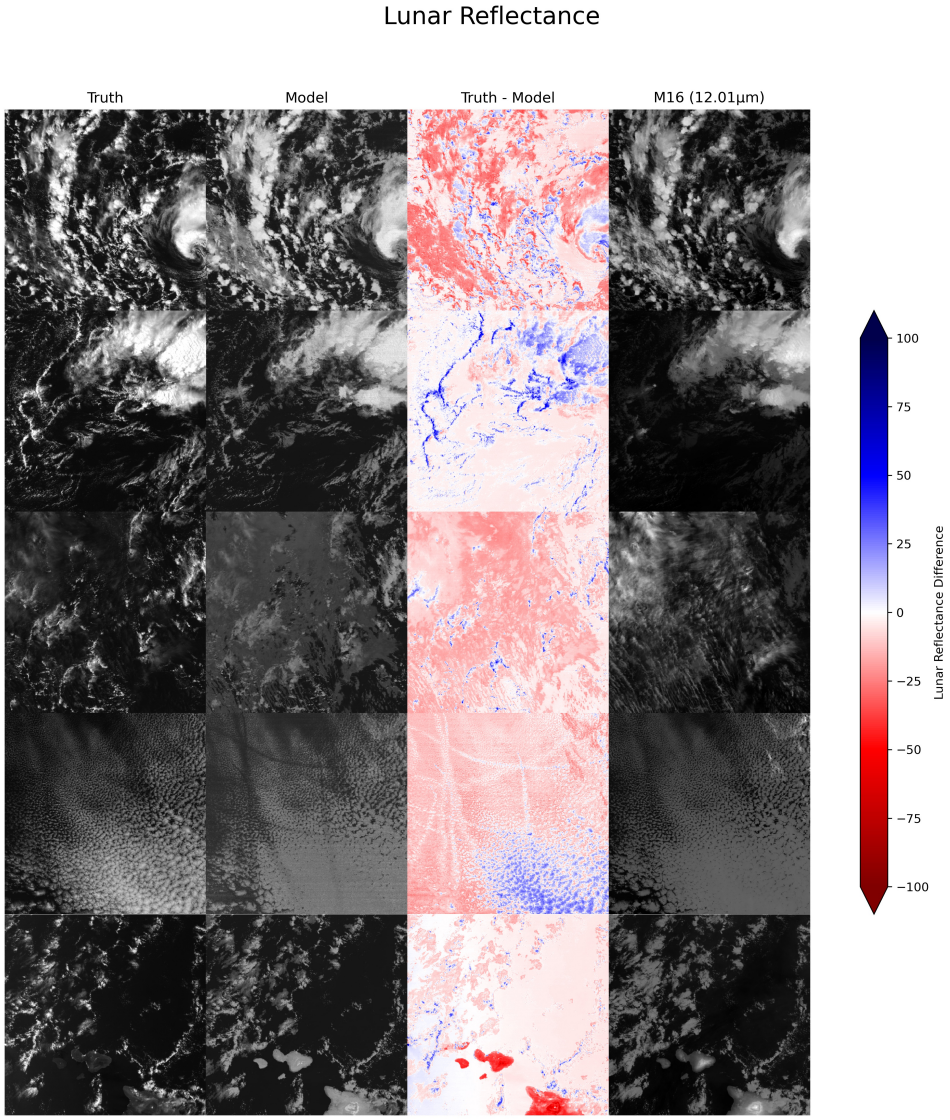

Figure 2.6: Qualitative Comparisons (Left to Right) of images from DNB radiance calculated lunar reflectance, predicted lunar reflectance, lunar reflectance differences between truth and predicted values, and VIIRS 12.01 µm channel for various scenes.

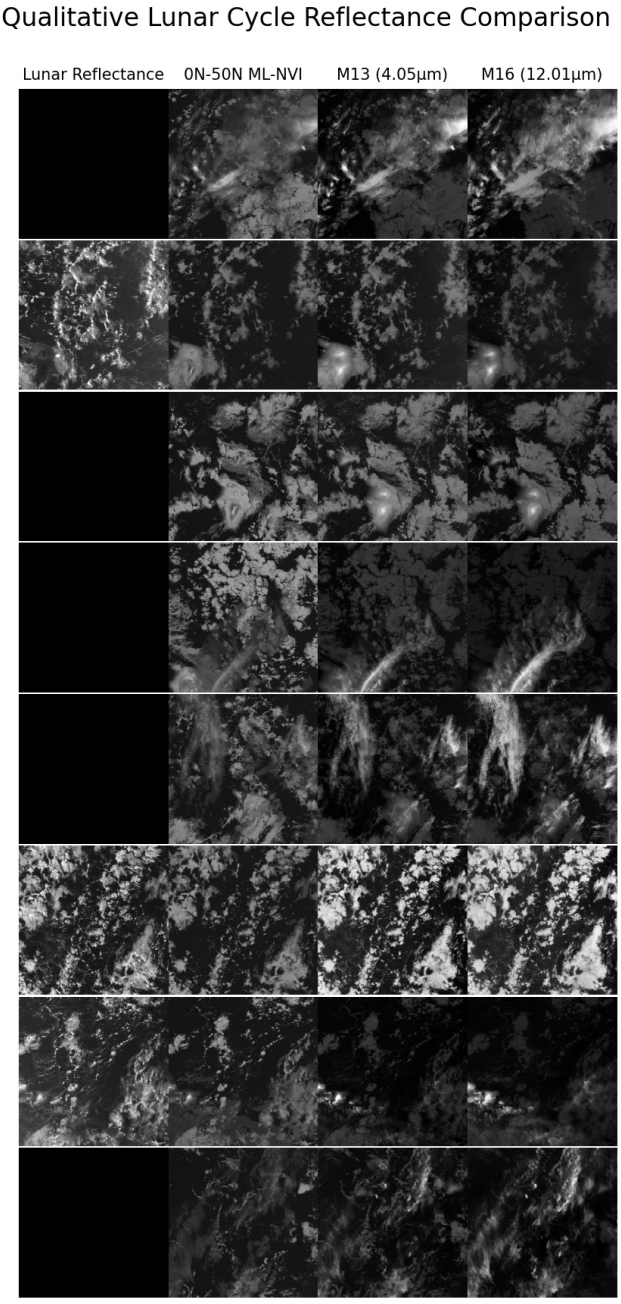

Figure 2.7: Qualitative Imagery Comparisons (Left to Right) of True DNB Lunar Reflectance, Full-Latitude Model Lunar Reflectance, and sensor radiances for VIIRS M13 (4.05 μm) and M16 (12.01 μm) for May 25, 2000 - July 18, 2000 covering 1.5 lunar cycles with high illumination present in rows 2,6,7.

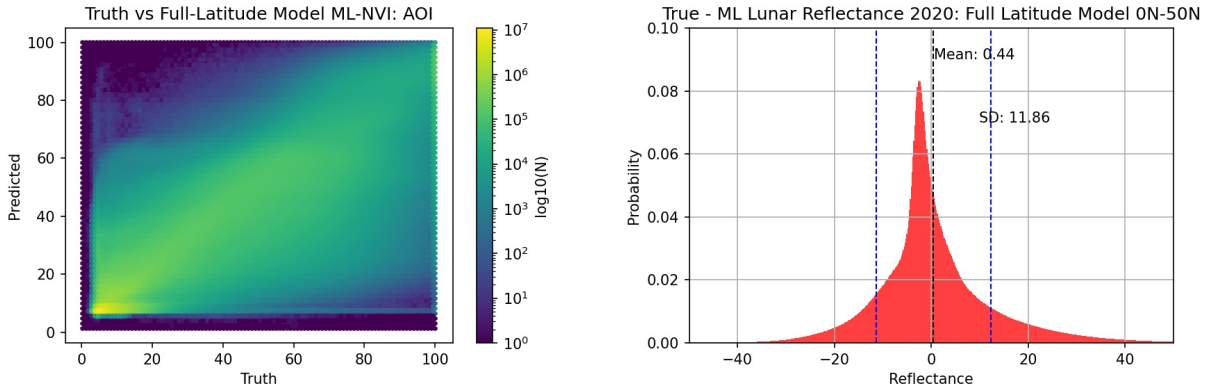

(a) True vs VIIRS Model Lunar Reflectance

(b) True - Predicted Lunar Reflectance

Figure 2.8: Lunar Reflectance Comparisons. Left: Data comparison of the 2020 validation data and the DNB true lunar reflectance for the full latitude VIIRS model over the 0N-50N AOI. Right: DNB true lunar reflectance minus full-latitude model reflectance evaluated at 0N-50N AOI.

Chapter 3

Improving Data Latency for Nighttime Visible Imagery: Transitioning Nighttime Visible Imagery from the JPSS VIIRS to the GOES ABI

3.1 Introduction

In 1947 the newly formed United States Air Force conducted a study to assess whether aerial reconnaissance could be done from Earth orbiting satellites. From this, Greenfield and Kellogg posited the feasibility of using such a satellite to gather meteorological information as well. In the unclassified version of their final 1951 report they highlighted that:

> A major advantage of satellite weather observations is the repeated broad spatial coverage. Such broad coverage provides the meteorologist with an essential element for his analysis, which is generally referred to as continuity. It permits him to follow a given system as it moves and develops over a period of days...not only may it then be tracked across an inaccessible area like an ocean, but any over-all changes or modifications that affect the visible parameters may be almost immediately noticed (Greenfield and Kellogg, 1960).

From here meteorological remote sensing via satellites rapidly developed. The first public satellite image, a low-resolution visible image, was processed on December 6, 1966 (Suomi and Parent, 1968). In October 1975, the first IR image was processed and made nighttime observation of Earth possible from space (Davis, 2007). In 1975 GOES-1 became the first operational geostationary meteorological satellite and provided an infrared (IR) sensor with 9km resolution and revisit time of 20-30 minutes (Stephens, 1994; Kidder and Vonder Haar, 1995). All satellite imagery provides benefits to weather forecasters, however, advances in remote sensing from geo-

stationary satellite have proved especially critical as forecasters can track and anticipate changes to weather phenomena with high temporal resolution over a large geographic region as outlined in Greenfield and Kellogg (1960).

The latest satellite employed by the United States, the GOES Advanced Baseline Imager (ABI), is a 16-channel imaging radiometer with several similar bands to Japan's Advanced Himawari Imager (AHI) and the European Organization for the Exploitation of Meteorological Satellites (EUMETSAT)'s Spinning Enhanced Visible and InfraRed Imager (SEVIRI). This standardization across platforms enables enhancements to be used for more than one satellite permitting a more global coverage of the product. The standard operating scan mode for the ABI provides updates to the three primary sector elements as follows: full disk (10 min), CONUS (5 min), mesoscale (1 min) with a resolution between 0.5km and 2km depending on wavelength. The ABI provides an order-of-magnitude improvement for environmental monitoring from the previous GOES series and is has improved significantly over the last 45 years (Schmit et al., 2017).

Though gaining visibility and traction in recent years, nighttime "visible" imagers have been around since the 1960s. The Defense Meteorological Satellite Program (DMSP) Operational Linescan System (OLS) was designed "to create simple imagery for human interpretation for night (Lee et al., 2006)." Nighttime detection of clouds improved again with the evolution of the NPP VIIRS Day/Night Band (DNB) which takes advantage of both the visible and IR spectrum and provides radiance measurements over eight orders of magnitude utilizing lunar illumination and airglow as its light source (Miller et al., 2013; Liang et al., 2014; Seaman and Miller, 2015; Zinke, 2017). The DNB provides one nighttime overpass of a tropical/mid-latitude site per satellite with 375m resolution at nadir and enables radiance collection from 500nm to 900nm. Postprocessing radiance scaling done to make usable imagery includes the near constant contrast (NCC), ERF-dynamics scaling, and high near constant contrast (HNCC) (Baker, 2013; Seaman and Miller, 2015; Zinke, 2017). The Miller-Turner Lunar Reflectance model enable transformation of radiances to a lunar reflectance value (0-1) which provides visible imagery and retains the satellite measurement; however, it is only available for approximately 2 weeks of the lunar cycle and with

high lunar elevation angles (Miller and Turner, 2009; Miller et al., 2013). Lunar reflectance and pseudo albedo can be used in methods similar to that used for solar reflectance, but its source reflectance is at a much lower intensity and somewhat different wavelength distribution, so it is not a direct substitution for solar reflectance and albedo values for cloud and ground properties (Miller and Turner, 2009; Miller et al., 2013). Albedo is not a proxy for cloud cover amount though visually it helps distinguish between cloud free and cloudy scenes.

Satellite imagery provides critical information for continuous monitoring of cyclones and tropical cyclone (TC) forecasting. Properly locating the center of the cyclone's rotation is one of the key elements critical for nowcasting track and intensity. While only available during daylight hours, visible channels have proven the most reliable channels for tropical storm monitoring (Wimmers and Velden, 2016). Miller et al. (2006) demonstrated that correct position identification of the LLCC was improved by 60-120 nautical miles over IR imagery with the OLS. The DNB improved position identification further, but its revisit time is problematic. Miller et al. (2013) and Hawkins et al. (2017) highlight many examples using DNB lunar reflectance during periods of darkness to enhance TC forecasting. DNB is especially useful for tracking storm circulation because it is able to "see through" upper level cirrus and find the mid-to-low circulation patterns and help assess the amount of shear in the environment which in turn not only improve track but intensity forecasts as well (Hawkins et al., 2017). In his chapter on GOES-R Applications to Hurricane Monitoring, Velden (2020) posits that improved LLCC identification from nighttime visible imagery would improve numerical weather prediction modeling. The National Hurricane Center uses night-time visible imagery products for tracking storms and Joint Typhoon Warning Center (JTWC) cyclone forecast discussions state that estimates of storm center have improved with the DNB RGB imagery on multiple occasions (Hillger et al., 2016; Chirokova et al., 2018; Velden, 2020).

Satellite imagery is a key asset in fog detection and also aids in the timing of regional and point specific fog dissipation which can in turn ensure the safety of many resources such as airports, roads, and shipping lanes. Additionally, the optical depth of fog banks can further assist to determine which region may clear sooner due to daytime heating and localized circulation patterns

(Gurka, 1978b,a). Surface clouds are especially difficult to visualize in the IR as they have a similar BTs as the Earth's surface (Ellrod, 1995). Bispectral differencing can be used to determine composition (ice or water) and cloud droplet size which helps constrain cloud height and optical depth (Liou, 2002). Brightness temperature difference (BTD) calculations between short wave IR (SWIR) near 3.9 μm and long wave IR (LWIR) between 10.3 μm and 11.1 μm are the most common BTDs applied due to the spectral responses of droplet phase and droplet size at these wavelengths which are used to optimally highlight low-level cloud features, especially at night (Ellrod, 1995; Cermak and Bendix, 2005; Calvert and Pavolonis, 2010). A brief review of cloud spectral properties in the IR can be found in Pasillas et al. (2023) (in review). Several products for cloud detection exist, but the visual results are often scaled images using color to represent features versus displaying what the features would look like to the human eye. Nighttime visible imagery products are more intuitive, similar to daytime visible imagery, with white clouds, and cloud height and optical depth can be inferred from layered cloud types and reflectance values.

Tropical cyclone and fog monitoring are two examples of the benefits that nighttime visible imagery can provide, but many applications benefit from continuous observations from satellites. Miller et al. (2013) thoroughly covered the benefits of the DNB and nighttime visible products and posited improvements to both the research and forecast communities as well as the technical limitations from a geostationary nighttime imager. Huang et al. (2014) provides a meta-analysis on the growth of publications surrounding the DMSP OLS prior to the operationalization of the DNB demonstrating the rapid growth in the interest of nighttime visible and low-light imagery. Ensuring quantitative measurements in a nighttime lunar reflectance product enables the ability to improve cloud particle size detection and optical depth when spatially and temporally collocated with IR; a synthetic lunar reflectance value may have the same added benefits (Miller et al., 2013; Levin et al., 2020). The remainder of this chapter examines the development, testing, and validation of the GOES ABI NVI (A-NVI) as the VIIRS model (V-NVI) is translated for use with ABI. Section 2 reviews data and channel selection as well as model architecture. Section 3 is the general

validation of A-NVI. Section 4 provides demonstration and application for geostationary nighttime visible imagery, while the summery and conclusions close out Section 5.

3.2 Data

We used JPSS NOAA-20 and GOES-17 data over the open northern Pacific Ocean from December 2019 – November 2020 corresponding to the date of a full moon +/- 1 day for the validation of the model utilizing GOES ABI. As the model has been previous validated, no additional training and testing data was necessary. We retained the area of interest (AOI) contained by latitude 0N to 50N and 180W to 127W over the open oceans as seen by the dark black box in Figure 3.1. This minimized complications from city lights over land and accounted for various background sea surface temperatures (SSTs) as well as enabled comparisons to the previous validation data set from the initial model validation on VIIRS. For GOES ABI validation, data was limited to rows of 1200 pixels centered on DNB nadir and the associated ABI data in the AOI. GOES-17 loop heat pipe issues impacted channel quality during this period. Utilizing the Focal Plane Model temperature predictions charts and known cooling activation dates we reduced the 2020 full moon cycle data set from 13 to six sets that are free of known errors (Fiore and Seybold, 2021). Data for this research was retrieved from the National Oceanic and Atmospheric (NOAA) Comprehensive Large Array-data Stewardship System (CLASS) server (https://www.class.noaa.gov/).

Spectral bands on the VIIRS and ABI, though similar, are not identical, and have different widths and central wavelengths. A depiction of the VIIRS and ABI bands overlayed on a standard atmosphere transmission profile can be seen in Figure 3.2. Intercalibration between VIIRS and ABI sensors for some channels is tracked at the NOAA Center for Satellite Application and Research (STAR) Integrated Calibration and Validation System (ICVS). They demonstrate that there is typically a less than .15 Kelvin difference in the brightness temperature measurements between ABI channels 07 (3.9 μm), 11 (8.4 μm), and 13 (10.3 μm) when compared to VIIRS bands M13 (4.05 μm), M14 (8.55 μm), and M15 (10.76 μm) respectively with the greatest differences being in the SWIR comparisons. Although the channel spectra overlap, the ICVS does not do routine

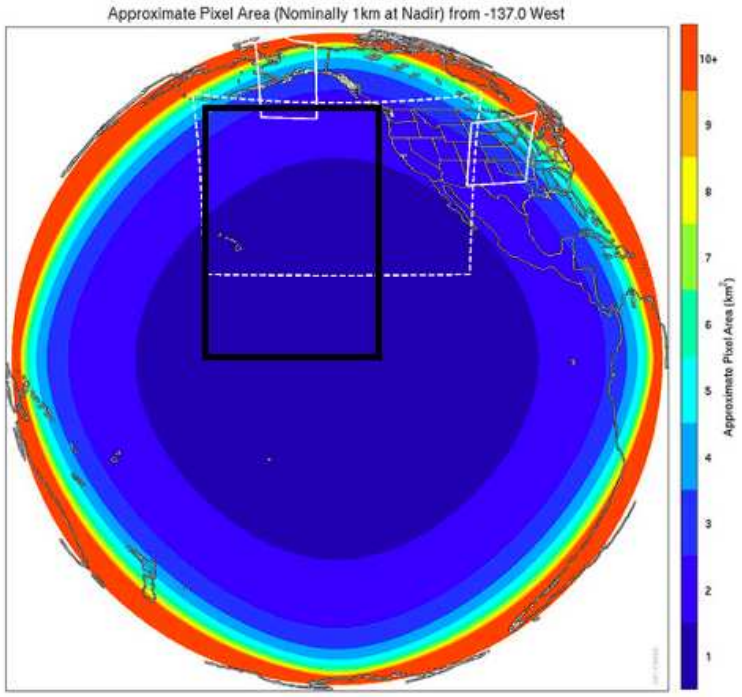

Figure 3.1: Depiction of the GOES 17 ABI sensor footprint and associated pixel size for the full disk, CONUS, and mesoscale scenes. The black box highlights the study area of interest. Figure modified from (Schmit et al., 2017) Fig 5.

assessment of VIIRS M15 (10.76 µm) and ABI channel 14 (11.1 µm) nor between VIIRS M16 (12.01 µm) and ABI channel 15 (12.3 µm). We created lunar reflectance predictions using both ABI channel 13 and 14 substitutions to match VIIRS channel M15 to assess if there is a preference for substituting one band over the other due to its spectral response. While there is no routine assessment of VIIRS M16 to ABI channel 15, we chose this band substitution based on the overlapping spectral response functions as seen in Figure 2.2. Though centered at different wavelengths and with different spectral widths, the impact on this selection is limited as cloud absorption is relatively flat across the spectrum. Additionally, NOAA STAR ICVT intercalibration demonstrations and other studies show differences between these channels for VIIRS and ABI are far less than a 1K difference at 300K permitted for inter-satellite calibration limits (Gunshor et al., 2004; Chander et al., 2013; Huang et al., 2020; Lee and Ahn, 2021). For these reasons we chose direct substitution between our chosen VIIRS and ABI sensors without transforming them

to common pseudo-wavelengths or adjusting the spectral representation of ABI channels to VIIRS wavelengths and channels. The VIIRS and ABI channels, corresponding central wavelengths, and associated prior research with brightness temperature differences can be seen in Table 3.1.

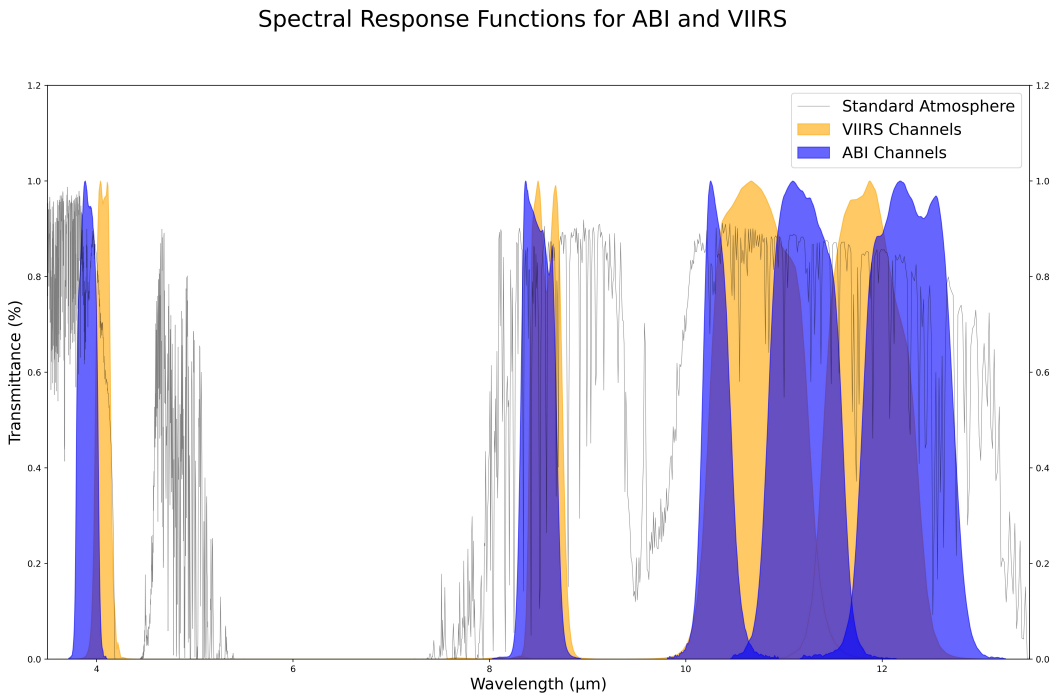

Figure 3.2: MODTRAN standard atmosphere profile from 3-14 μm with spectral response functions for the JPSS VIIRS (orange) and GOES ABI (blue) channels overlaid.

In order to do quantitative validation of GOES lunar reflectance values against the DNB lunar reflectance, ABI radiances need to be collocated (in time and space) with the DNB lunar reflectance. A function was created to evaluate and temporally match data between GOES and VIIRS date-time groups (DTGs). Concerns arise in intersatellite comparisons with view angles, sensor distance and parallax, especially between a geostationary and polar orbiter (Gunshor et al., 2004; Chander et al., 2013; Huang et al., 2020; Lee and Ahn, 2021). As seen in Figure 3.1 as one moves away from nadir on GOES, the footprint for the pixel increases in size with the best data resolution between 40N and 40S, degrading in all directions away from the subsatellite point. Radiance value adjustments for any view or solar angle are conducted in the processing to L1b data and the values mapped to the ABI grid represent nadir values and do not need to be further modified (Carlomusto,

Table 3.1: VIIRS moderate band central wavelengths and brightness temperature differences with the corresponding ABI bands central wavelengths and brightness temperatures differences used in training and validating the nighttime visible imagery (NVI). Previous research conducted for cloud detection on the brightness temperature differences is provided in the far right column.

VIIRS Band	VIIRS Central Wavelength	ABI Band	ABI Central Wavelength	Prior Research Use
M13	4.05	C07	3.9	
M14	8.55	C11	8.4	
M15	10.763	C13 / C14*	10.3 / 11.1	
M16	12.01	C15	12.3	
M13M14 BTD	4.05 - 8.55	C07C11 BTD	3.9-8.4	
M13M15 BTD	4.05 - 10.763	C07C13 BTD or C07C14 BTD	3.9-10.3 or 3.9-11.1	3.9 and 10.35 Legacy fog product (Ellrod 1995, Ellrod and Gultepe 2007) Wetzel et al 1996, Bendix 2002, Hillger 2008, Miller et al 2022 3.75 and 10.8 (Kim and Hong 2019)
M13M16 BTD	4.05 - 12.01	C07C15 BTD	3.0 -12.3	3.75 and 12 (Kim and Hong 2019, Anthis and Cracknell 1999)
M14M15 BTD	8.55 - 10.776	C11C13 BTD or C11C14 VTD	8.4-10.3 or 8.4-11.1	8- -11- (Strabala and Ackerman 1994)
M14M16 BTD	8.55 - 12.01	C11C15 BTD	8.4-12.3	
M15M16 BTD	10.763 - 12.01	C13 C15 BTD or C14C15 BTD	10.3-12.3 or 11.1 -12.3	10.3 and 12.3 (Prabhakara et al 1974, McMillin 1975, Inoue 1989, Strabala and Ackerman 1994, Stephens 1994, Lindsey et al 2014)

2019; EUMETSAT, 2010; Yu et al., 2021). Furthermore, Huang et al. (2020) demonstrated that these values are also very consistent among available geostationary sensors. No adjustments to the SWIR need to be made for nighttime use as there is no solar contributions in the validation data set, and the SWIR is purely transmissive. If the model is applied to daytime or transitional periods such as sunset and sunrise, calculated lunar reflectance values will assume that values are all from transmission and imagery will appear different due to the contribution from the solar reflectance in the 3.9 μm band. Satpy, the software used to geographically collocate the data to the DNB data set based on our temporal matching, conducts the necessary calculations to convert satellite measured radiances to brightness temperatures using the Planck function and sensor coefficients (PyTroll, 2009-2022).

3.3 Machine Learning and Architecture

With increased data availability, computing power, and memory storage, there have been many attempts to create synthetic nighttime "visible" imagery due to the extensive uses highlighted above

(Chirokova et al., 2018; Kim et al., 2019; Kim and Hong, 2019; Mohandoss et al., 2020; Harder et al., 2020; Cheng et al., 2022; Pasillas et al., 2023). Many of these studies have been aimed at specific meteorological features (cyclone, fronts, fog, etc) and have been qualitatively compared to single channel IR data or visible RGB during daylight. Data and imagery derived from DNB radiances are the best representation of nighttime "visible" imagery and were used in both Chirokova et al. (2018) and Pasillas et al. (2023) products. All studies with quantitative validation approached the problem differently (metrics, scene types, etc) leading to challenges for quantitative product inter-comparison. Pasillas et al. (2023) provides qualitative imagery and quantitative baseline metrics for lunar reflectance in its VIIRS NVI (V-NVI) and serves as a launching point for the creation and validations of the ABI Nighttime Visible Imagery (A-NVI) and its associated lunar reflectance values.

The model used is a fully connected neutral network that was trained on full moon VIIRS data from 0N to 50N and 127W to 180W longitude. For translation from VIIRS to ABI there are no adjustments to the model architecture: the layers, nodes, activation functions, epochs, and batch sizes remain unchanged. The only change is in the predictors to account for the ABI channels. The model used is a fully connected feed forward neutral network and its architecture can be seen in Figure 3.3. There are 10 inputs as seen in Table 3.1 which are determined from the VIIRS to ABI channel relationships highlighted in Figure 3.2. To note, ABI channel 13 and channel 14 values and brightness temperature differences (BTDs) associated with them are not used simultaneously; models were run with 10 predictors as with the VIIRS and these channels were used interchangeably to assess the qualitative and quantitative differences.

3.4 GOES ABI Validation

Imagery validation typically consists of two phases, a qualitative assessment of the imagery and quantitative assessment against a truth and comparison to prior results. Pitts and Seybold (2010) outlines the NOAA-NASA process for evaluating satellite imagery. To assess the impact of using ABI channels in lieu of VIIRS bands, qualitative imagery comparisons are conducted

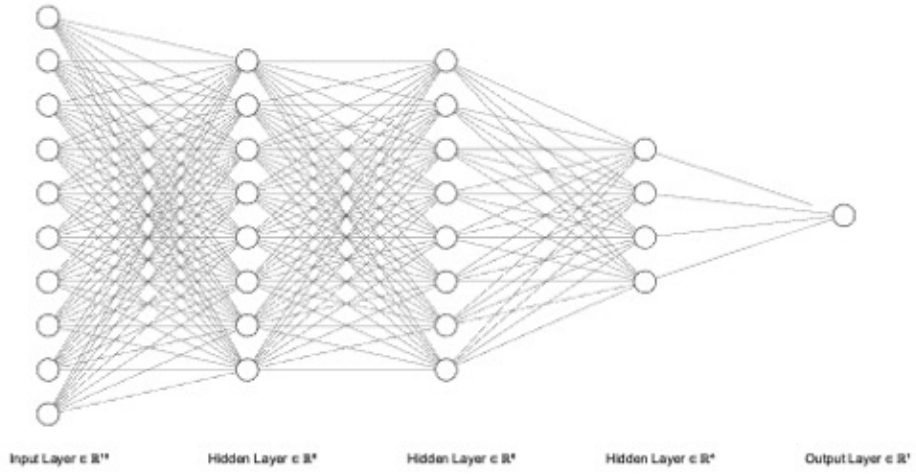

Figure 3.3: Model Architecture for the Nighttime Visible Imagery (NVI)

against DNB lunar reflectance at the full moon. Retrieved cloud properties will only be as accurate as the resolution of the channels it receives data for which may degrade actual information as these phenomena vary at smaller resolutions than satellite data can provide even if they are collocated. Because of this, imagery created by GOES ABI will be less clear and may have less accurate lunar reflectance values due to the resolution differences between the VIIRS DNB, VIIRS M-bands, and the GOES ABI channels. After comparisons to true lunar reflectance are conducted, imagery from both GOES predicted lunar reflectance runs are compared to the results of V-NVI for an assessment of how the model handles the chosen wavelength substitutions and versus ABI IR to ensure there is enhanced detection of weather phenomena over IR alone.

Figure 3.4 shows qualitative comparisons but includes regions outside of the quantitative validation AOI. The four rows represent four illustrative cases. The lunar reflectance and V-NVI are at a footprint of 375m while the ABI footprint is 2km so there will be a loss of spatial resolution from VIIRS to GOES. However, the transfer enables continuous coverage versus once or twice nightly passes which is the frequency for lunar reflectance and the V-NVI. The DNB true lunar reflectance is the highest quality of imagery possible with respect to spatial footprint and wavelengths. The V-NVI represents the best qualitative imagery we can expect from the model as its inputs come from the exact same time and view angle as the DNB. The two C-band A-NVIs high-

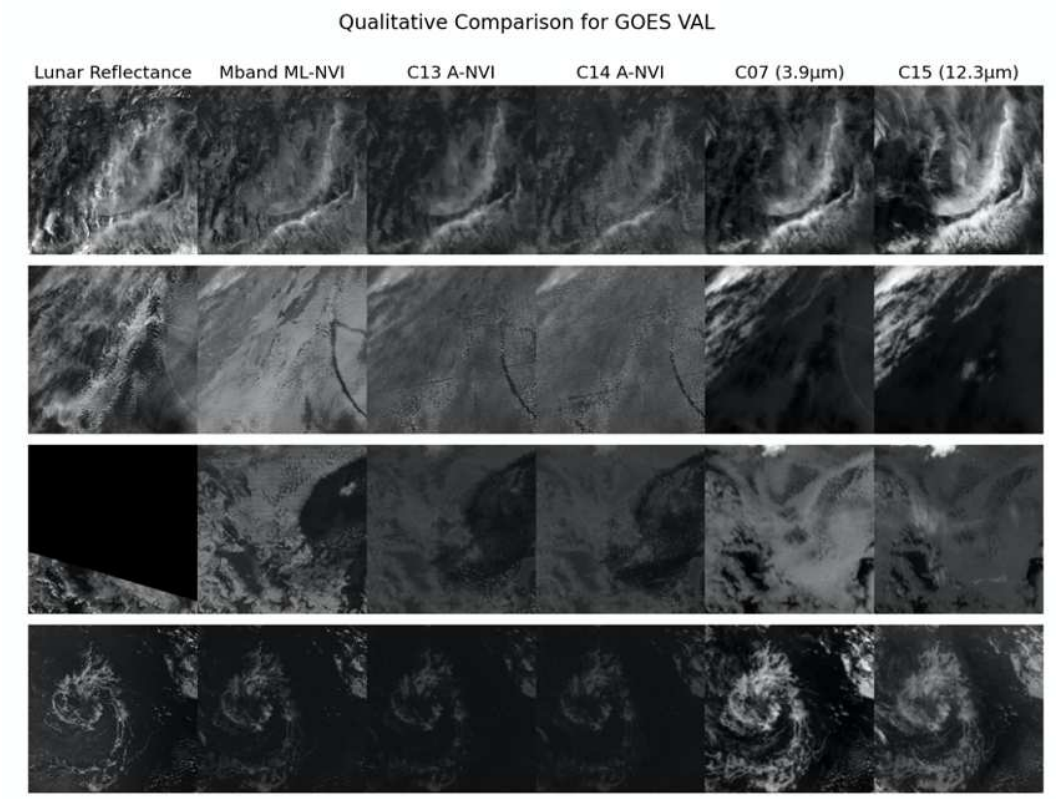

Figure 3.4: Qualitative comparison for the 2020 GOES ABI Nighttime Visible Imagery Validation. For each case, from left to right are the DNB true lunar reflectance, V-NVI, C13 A-NVI, C14 A-NVI, ABI Channel 07 (3.9 μm), and ABI Channel 15 (12.3 μm).

light the difference in image quality using ABI channel 13 versus channel 14 for a substitute of M15. Infrared images at ABI channel 07 and 15 wavelengths are used to demonstrate what current sensing ability is possible for these scenes at the lowest and highest observed IR wavelengths that are shared between the VIIRS and ABI sensors. Overlapping wider wavelength bands, differing central wavelengths (especially in the 3.8-4.0μm range), view angle, and sensor distance account for the main differences between the V-NVI and A-NVI imagery. One of the greatest visual differences between the two GOES A-NVIs and the V-NVI is the gradient. The V-NVI has strong contrast like the DNB lunar reflectance, but both GOES A-NVIs have weak contrast in the lunar reflectance, though they are similar to each other. In rows 1 and 2 the cirrus is more prominent in the IR than in any of the NVI models and with its removal we can see lower clouds better in the models than in IR. Row 2 shows upper level cirrus cloud over large stratocumulus sheets. In the IR the stratocumulus looks rather uniform but looking at the DNB lunar reflectance it is clear they are

not and are mainly comprised of open cell cumulus which is more indicative of precipitation than closed cell. The A-NVI can capture the texture and help to delineate between the open and closed cell stratocumulus and highlights ship tracks more clearly as well. This allows viewers to make better assumptions about existing atmospheric dynamics and stability profiles and precipitation. Row 3 shows how lunar reflectance is only available for part of the period, but the models fill in what should be there. There is clearing of cloud in the right-hand side of the models that is missed in the IR which can help to delineate where the cloud boundaries are located. In the last row a low pressure region can be seen in the lunar reflectance. While it is observable in all images, the NVI images help remove the upper-level cloud to reveal the circulation pattern better.

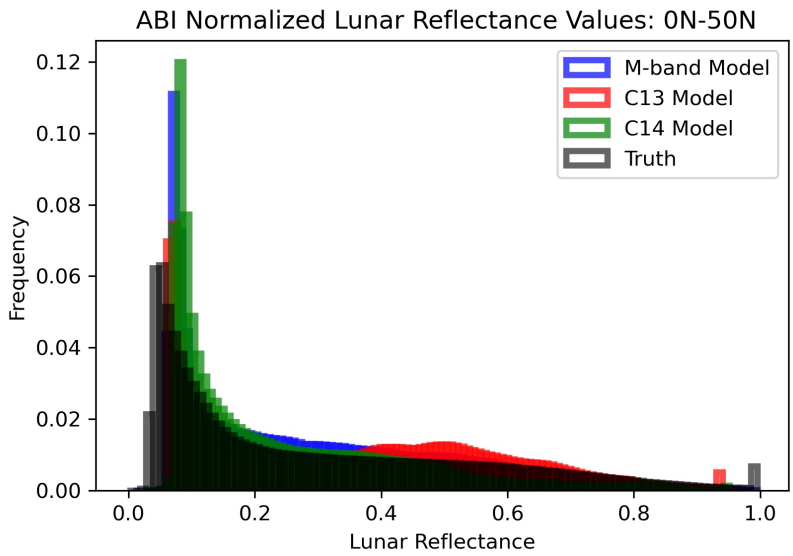

Figure 3.5: Normalized lunar reflectance values for the observed lunar reflectance (grey), VIIRS-NVI (blue), C13 A-NVI (red), and C14 A-NVI (green) over the ABI-NVI validation area of interest.

The probability density functions (PDF)s of true lunar reflectance versus lunar reflectance from the three model predictions (V-NVI, C13 A-NVI, C14 A-NVI) are seen in Figure 3.5. Both C13 A-NVI and C14 A-NVI have similar PDFs but they differ from the truth and V-NVI. The PDFs demonstrate that the gradient difference is due to the disparity in forecasting lunar reflectance values between V-NVI and the A-NVI, especially in forecasting lunar reflectance values between

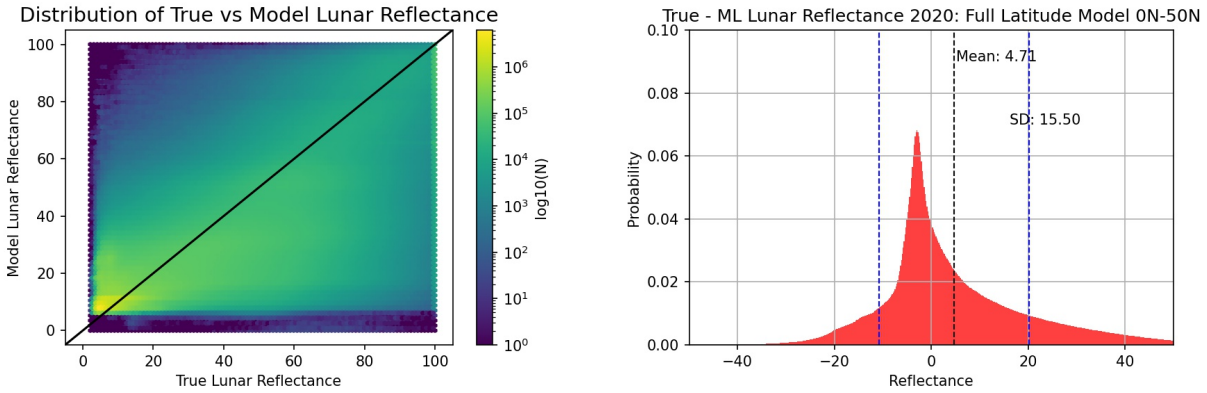

(a) True vs Model Lunar Reflectance Distribution

(b) True - Predicted Lunar Reflectance

Figure 3.6: Scatter plots of the observed vs A-NVI predicted lunar reflectance(left) and histogram of the observed minus predicted lunar reflectance(right).

.15 and .35. Based on the qualitative imagery comparisons, sensor intercalibration demonstrations from previous research, and findings seen in Figures 3.5 - 3.6, and Figure 3.4, A-NVI with the ABI channel 13 appears to perform somewhat better that the channel 14 product and is used henceforth. The "C13" prefix will be dropped and the A-NVI created with ABI channel 13 will be referred to as the A-NVI for further analysis and discussion.

Following the qualitative assessment, quantitative metrics were calculated against the DNB lunar reflectance at full moon periods for the validation AOI for both V-NVI, and the A-NVI lunar reflectance values. This enables comparisons to the truth and to V-NVI which is, in theory, the best performance we can expect to achieve for the situation as the model moves to a new platform and sensor. Regions of zero lunar reflectance in the validation data due to the lunar angle being below the threshold used in the Miller Turner lunar reflectance calculations are kept in the visual comparisons but removed to prevent bias for statistical validation. Quantitative scores seen in Table 3.2 utilize the full range of data and do not consider the distribution of data itself. Value difference plots for A-NVI and lunar reflectance highlights a mean of 4.7 and a standard deviation of 15.5. Combining this information with the scatterplots seen in Figure 3.6 shows that the A-NVI model tends to overpredict values at high lunar reflectance and under predict reflectance values at lower lunar reflectance values. This highlights that there is opposing bias in the A-NVI depending

on the feature of interest. The explained variance and R2 scores sit at 0.58 and 0.55 respectively, however, as seen in Table 3.2, the values for the V-NVI for the same data set are both 0.75 thus when compared to the max achievable scores it continues to explain a large level of variance even with the wavelength differences between the VIIRS and ABI sensors. A RMSE of 16.2 and MAE of 11.1 is reasonable when viewing lunar reflectance values from a cloud categorization perspective and our difference plots indicated that most of this error occurs when predicting reflectance values less than 0.2. The Spearman's coefficient and correlation coefficient demonstrate there is high correlations between the true lunar reflectance and the model trained reflectance with 0.77 and 0.76 values respectively. Due to the nature of the machine learning model chosen, these values are based purely on spectral relationships and not spatial correlation. A Jensen Shannon Divergence (JSD) score of 0.18 further highlights the similarity between the data sets and is indicative that the A-NVI would be a reasonable substitution in the absence of true lunar reflectance.

Table 3.2: Quantitative metrics for the 2020 validations area of interest for the V-NVI, C13 A-NVI, and C14 A-NVI (left to right).

VALIDATION ML DATA	Explained Var	R2	RMSE	MAE	Spearman Coor	Corrcoef	JSD
VIIRS	0.7486	0.7486	12.05	8.376	0.86	0.8645	0.1426
GOES C13	0.584	0.546	16.20	11.14	0.765	0.764	0.184
GOES C14	0.576	0.543	16.25	11.23	0.753	0.76	0.187

3.5 Demonstration of Forecasting Uses for A-NVI

An examination of the imagery is visually appealing and provides baseline validation metrics, but its ultimate goal lies in its utility. A-NVI is usable with data across all GOES fields of view: full disk, CONUS, and mesoscale and transferring to GOES increases the temporal resolutions from two to four passes per night to providing updated imagery as frequently as every minute in mesoscale fields. Accessible across the various scan strategies and sensing domains, the product

can be used for short range forecasts and providing global continuity for the long wave pattern and large mesoscale features. Two key uses of this imagery include fog forecasting and tropical cyclone forecasting.

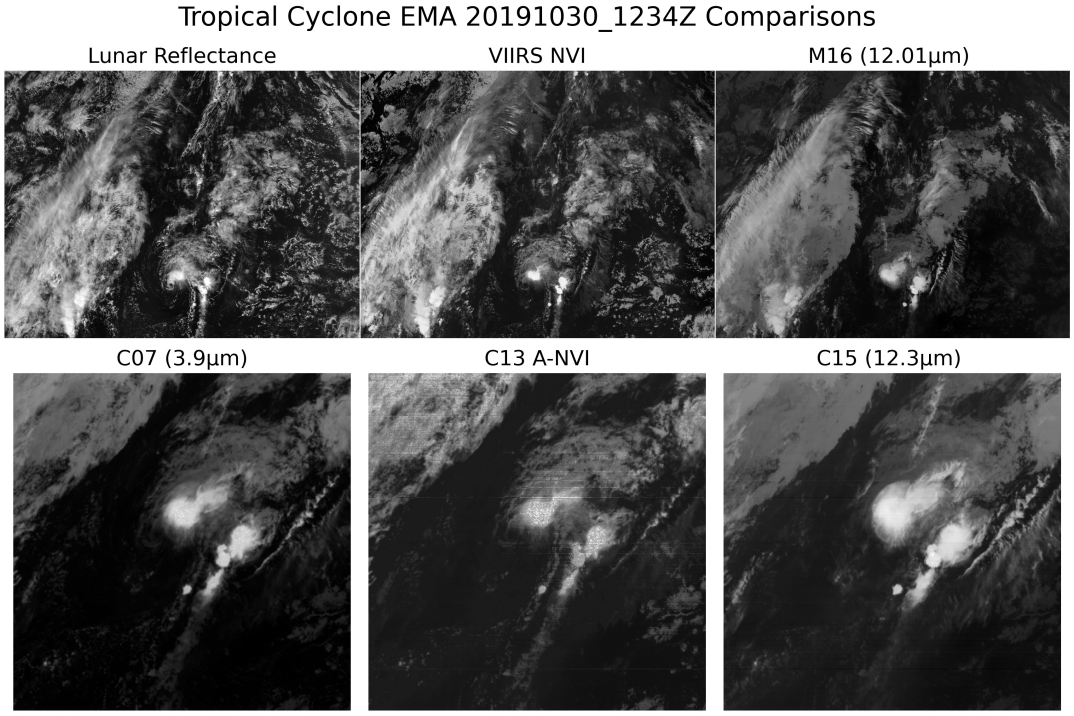

Figure 3.7: Qualitative comparisons for Tropical Cyclone Ema between true lunar reflectance, V-NVI, M15 (top row, left to right) and ABI channel 07, A-NVI, and ABI channel 15 (bottom row, left to right) to highlight footprint and wavelength resolution differences.

Forecasters have difficulty identifying low level circulation of tropical cyclones under various conditions: when layered upper-level clouds cover lower cloud, at night in IR when there is low thermal contrast, in areas of shear, and when the storm lacks a well-developed eye. The low-level circulation is key for an accurate position while the distance in the decoupling of a storms upper and lower circulation is a proxy measurement of the amount of shear the system is in and the level of tilt the vortex has. Both have implications on strengthening or weakening of a system. If available, the Joint Typhoon Warning Center uses RGB composite imagery that combines the VIIRS DNB with IR during nighttime TC analysis which improves detection in these situations but when not available their primary tool is animated geostationary IR (Hillger et al., 2016; JTWC, 2018).

A-NVI can expand temporal coverage of this RGB. Figure 3.7 shows qualitative comparisons for Tropical Cyclone Ema. Looking at VIIRS channels only (top row), the low level circulation is apparent in both the lunar reflectance and the NVI but lacking in the IR. Applying the model to the ABI (bottom image middle column), one can still capture the cloud features, to include the appearance of a low level circulation, in the A-NVI even with the decreased resolution and animation would improve its detection. Having the VIIRS and ABI images side by side demonstrates the importance of satellite view angle and proper projection of grids when looking at TC circulation as highlighted by the small, almost circular cloud and cloud line present in the lower right corner of the viewing boxes. Displacement and remapping of images such as this can be corrected through methods of latitude and longitude conversion and feature height assignment as outlined in Wimmers and Velden (2016).

Fog forecasting has its own challenges which are exacerbated at night. Limited thermal contrast between low clouds and the background scene, upper-level cloud obstruction, and even surface temperature inversions greatly impact the ability to detect and track fog via satellite. Figure 3.8 shows an extensive evening fog event off the coast of California at two different time steps. Rows 1 and 3 are the same time step but different views (1-mesoscale, 3-CONUS) and demonstrate how imagery may look in the ABI channel 07 (3.9 μm) and A-NVI if there is residual solar reflectance as the sun has not fully set at this time while rows 2 and 4 are in a period of full darkness and occur at the same time. Though trained on data sets where ABI channel 07 (3.9 μm) was fully emissive, artifacts will be seen like this if there is a reflectance component present. This is something for users to be aware of especially when looking at still images as the visual appearance of fog changes greatly once there is only reflective components in the SWIR. In the A-NVI there are three distinct cloud sets while the IR only shows two. Fog formation along the California coastline is visible in the A-NVI but not the IR because of this distinction. The change in appearance of the same features from sunlight to the overnight period of darkness are seen in the second and fourth rows. Comparing the A-NVI verses the two IR channels it is clear that upper lever clouds are best seen in AB channel 15 (12.3 μm) but that low clouds are most apparent in the A-NVI. The A-NVI captures

reflectivity and thickness of these low clouds and appear similar to visible imagery which provides spatial connotations through texture better than IR alone. Additionally, in both the CONUS and mesoscale A-NVI images the fog in San Francisco Bay, Monterrey Bay, and the Salinas Valley is much more prominent than in IR as seen by the white patches. When animated, this imagery will be especially useful to track the dissipation and development of fog events. Ship tracks are also apparent in the CONUS A-NVI but absent in the IR.

3.6 Summary and Conclusion

Satellite imagery and its increasing availability in temporal, spectral, and spatial resolution has greatly advanced the skill of forecasting meteorological events. Cloud identification by the human eye is most easily done in the visible spectrum, but limited to daylight hours. The JPSS DNB provides a capability similar to visible imagery at night using lunar reflectance and ambient light, however its poor temporal sampling limits its usefulness to short term forecasters. Attempts have been made to create a low-light visible product using machine learning with varying levels of success, demonstrating the need of such a product (Chirokova et al., 2018; Kim et al., 2019; Kim and Hong, 2019; Mohandoss et al., 2020; Harder et al., 2020; Cheng et al., 2022; Pasillas et al., 2023). The A-NVI is a proposed solution to the remote sensing low-light visible problem that addresses temporal, geographic, and lunar cycle restraints to the DNB.

This study provided insight to a FNN that was created and validated using JPSS data and applied to the GOES ABI. Qualitative imagery comparisons and quantitative baseline validation statistics for lunar reflectance were performed. Additionally, forecasting benefits of the product were highlighted in its ability to detect cyclone circulations and fog. Combined with intercalibration statistics by Huang et al. (2020), the ABI validation demonstrated that a single algorithm can be used with minimal inter-senor calibration and achieve similar results for the ABI, Advanced Himawari Imager, Advanced Meteorological Imager, Advanced Geostationary Radiation Imager, and SEVIRI sensors. This model enables the use of a single process for greater global coverage,

temporal resolution, and gradient visualization of a nighttime visible like imagery for use across the system of polar and geostationary satellites.

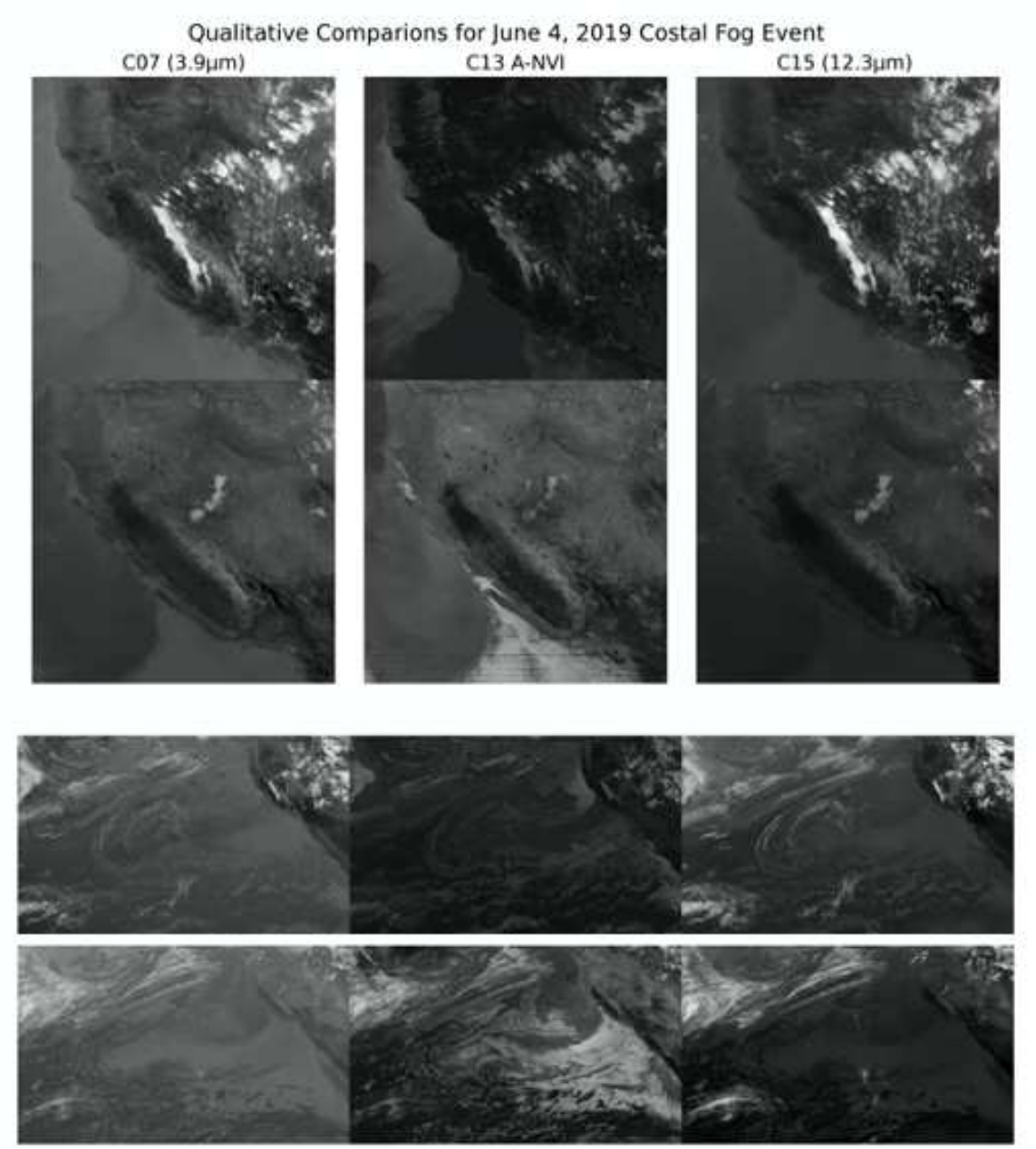

Figure 3.8: Qualitative comparisons between ABI channel 07 (3.9 μm), A-NVI, and ABI channel 15 (12.3 μm)(left to right) at mesoscale (row 1 and 2) and CONUS scale (row 3 and 4) view points.

Chapter 4

Improving the A-NVI and applications

4.1 Introduction

The benefits for nighttime visible imagery have been highlighted in prior studies and the ability to project such imagery from geostationary position will provide even more uses Miller et al. (2013); Chirokova et al. (2018); Kim et al. (2020, 2019); Kim and Hong (2019); Mohandoss et al. (2020); Harder et al. (2020). Nighttime visible imagery can see through upper level cirrus to track and place low cloud features and provide a more accurate 3D estimation of the environment than infrared imagery alone. It can assist forecasters with low cloud detection, tropical cyclone monitoring, sea ice detection, and even wind estimates from atmospheric motion vectors. As the NVI retains a quantitative derivation of raw measurements, it can aid in resolving the diurnal cloud cycle to improve global cloud climatology records and radiative transfer calculations for modeling, more so with its availability from geostationary satellites. In essence, it can be used in similar capacity to the DNB and is especially useful for the JPSS in the second half of the lunar cycle when lunar reflectances cannot be calculated and for geostationary sensors to provide forecasters nighttime visible imagery with the spatial coverage and temporal resiliency to accurately track mesoscale weather features in real time as they form and evolve. For the scope of this dissertation we will briefly mention general uses and places of substitution for NVI and then focus on tropical cyclone and nocturnal fog events. These cases will demonstrate the additional knowledge gained by NVI in two phenomena that research has shown via DNB that nighttime visible imagery can greatly enhance detection of and would further gain benefit from a geostationary product (Miller et al., 2013; Hawkins et al., 2017) .

4.2 Creation and General Uses for Nighttime Visible Imagery

The first step of the project was to train and validate a model for use with VIIRS M-bands. While this sensor suite has a DNB sensor, there are issues with lunar reflectance availability tied to the lunar cycle, and the ability to provide visually similar contrasting imagery across the day/night terminator line and with the lunar cycle as radiances measurements are modified by orders of magnitude. The V-NVI can replace DNB lunar reflectances for the period of reporting when the DNB lunar reflectance is not usable due to illumination or position for multi sensor imagery, model applications, and algorithms that use the DNB. This is especially helpful for polar winters when there is not enough ambient light for reliable visible imagery and thermal contrasts are hard to distinguish, a concept proven with National Weather Service Alaskan zone forecasters. The operational level 2b DNB Near Constant Contrast product still requires on screen scaling based on seasons and other factors, however the V-NVI provides a single full lunar cycle full time product that forecasters do not have to scale further in order to maximize the information which can save them time and training for feature detection and forecasting.

After training and validating a model for VIIRS, the V-NVI, the concept was applied and evaluated for use with the GOES ABI to exploit benefits that geostationary satellites have over polar equivalents including high temporal resolution and greater continuous geographic coverage. Any feature that is tracked on sub-daily scales will benefit with nighttime visible imagery. This product, the A-NVI, can provide a global nighttime view of clouds, allowing large scale feature tracking across the satellite domain. This will lead to better nocturnal cloud location and understanding. Finally, using satellite to detect low level circulation of tropical cyclones is the first step in providing position, intensity and structure updates as seen in in the JTWC reference notebook and Dvorak techniques with visibly imagery proving more accurate than infrared imagery (Miller et al., 2013; Hawkins et al., 2017; JTWC, 2018; Herndon et al., 2021).

Reviews of past weather events may help determine what went wrong for a busted forecast or to improve the understanding of underlying causes of extreme weather events in order to provide greater lead time and anticipation of future events. For National Weather Service Science and

Operations Officer Jon Zeitler a case study is meaningful if it meets two of the three following criteria:(i) a unique or rare occurrence of a weather event, (ii) a demonstration of how new or unusual observations can be used to identify, analyze, or forecast an event, and (iii) a demonstration of how theory can be applied, especially for unusual cases (Schultz, 2010). The main purpose of our case studies are to demonstrate a new observation method with the NVI. For the tropical cyclone cases, the second purpose is to address a challenging detection issue with respect to cyclone structure that has significant impact on forecasting. Similarly, though a common occurrence, addressing fog cases and low-lying clouds is done to bring light to a new product that may improve the forecasting for fog extent, thickness, and duration. Improving the detection of these features will reap dividends in the aim of weather forecasters to provide warning of significant weather phenomena to protect property and human life.

4.3 Cases

4.3.1 Tropical Cyclones

Tropical cyclone detection and understanding improved exponentially in the satellite era. It enabled the creation of the Dvorak Technique for estimating cyclone winds and pressure based on imagery patterns alone. Curved band, shear, central dense overcast (CDO), cold cover, and eye structure cloud patterns are not just pattern in imagery but also indicators of dynamical and structural changes, wind speed, and intensity of a system. When combined with trends, they can be used to determine if a storm is weakening or strengthening and the anticipated maximum winds (Dvorak, 1984). Created in the 1970s, the Dvorak Technique is the baseline for most cyclone intensity estimations from imagery to include the widely used Automated Rotational Center Hurricane Eye Retrieval II (ARCHER-II) algorithm (Velden et al., 2006). ARCHER-II is a near-realtime automated process that calculates a spiral score from cloud patterns, a ring score from microwave measurements for eye wall detection size, and a distance penalty to objectively determine where the low-level center of a storm is from various input imagery (Wimmers and Velden, 2016). Hawkins et al. (2017) asserts that using DNB TOA lunar reflectance in ARCHER-II to capture the surface

circulation and create spiral and ring scores would be advantageous as it could add details on shear information absent in the IR. Furthermore, it was assessed that GOES "fills gaps from polar orbiters with VIS(able) data being the best skill in center placement" (Wimmers and Velden, 2016). NVI can replace the DNB to provide similar data from both polar and geostationary views of storms.

We previewed annual storm reports from the 2017-2022 Atlantic and Pacific hurricane seasons in the GOES 16 and GOES 17 fields of view and reduced potential cases to those in areas of moderate to strong shear or where the National Hurricane Center (NHC) mentioned the use of nighttime visible imagery to enhance circulation detection. The tropical cyclone case presented is Tropical Cyclone Otis from the 2017 Pacific storm season. Illumination during this time decreased from 75% to 5% thus limiting the ability for DNB lunar reflectance imagery as the storm progressed. Post season storm reports indicated that its initial formation was poorly detected, with introduction into the tropical outlooks only 18hrs prior to formation, and that it was never expected to reach hurricane status. Not only did it reach hurricane status, it underwent rapid intensification and reached category 3, after which it moved into an area of environmental shear and rapidly deteriorated to a tropical storm less than 18hrs after becoming a hurricane.

Figure 4.1 shows cyclone Otis for the time leading up to and including initial tropical depression formation (TDF) with data from ABI channel 07, the A-NVI, and ABI channel 15 (left to right) at TDF -18, -6, -3, -0, and +3 hrs respectively) (top to bottom). Tropical depression formation was declared on September 11, 2017 at 6Z (4th panel) based on circulation present in a polar microwave overpass. The first row is 10/12Z and represents the time that the system was first included in any storm forecast products. In all three images we can see there is deep convection but no apparent circulation. The NVI has been designed to focus on low clouds thus the overshooting tops appear as a solid white cloud. The land ocean contrast provided can give contextual clues for the location of the storm that is missing in the IR. In rows 2 and 3 the NVI appears similar to ABI channel 07 but has more lower cloud captured. Row four corresponds to 11/06Z when a microwave pass capturing winds indicated that there was circulation present. This is a single pass with delayed revisit time that also may or may not capture the full cyclone system in its swath. This time is also

when differences between the IR images and the NVI become more apparent. Specifically we can see more cloud cover over the land over Central America and we can start to see some circulating low cloud to the right of the convection. This feature is not visible in ABI channel 15 (12.3 μm) and is faint enough it could be missed in ABI channel C07 (3.9 μm). The last row is three hours after the initial depression formation. The circulation is still not overly present in ABI channel 15 (12.3 μm) but is there in both ABI channel 07 (3.9μm) and the A-NVI, though again much more clear in the NVI. This time step shows how the convection transition from being at the center of the storm and where one may try to place an eye in IR imagery to the storm taking on a more asymmetrical shape with significant tilting of the system. Animations of these channels can track the clouds and identify the circulation best in the NVI. Tracking the low-level circulations location in relation to the convection over night in this imagery can assist to determine if the vortex continues to remain tiled or starts to stack and strengthen instead of waiting for daytime imagery.

Figure 4.2 shows Tropical Cyclone Otis for the time leading up to and including hurricane formation declaration (HD), with data from ABI channel 07, the A-NVI, GOES+NVI and ABI channel 15 at HD -6, - 3, and -0 hrs respectively. Again, it was polar imagery that aided in the decision to upgrade Tropical Cyclone Otis. On September 17, 2017, at 10Z Otis was upgrade to a category 1 hurricane based on identification of a mid-level low on a microwave imagery at that time. This sample also highlights two variations of the A-NVI, one with the ABI channel 13 that we have validated in the previous chapter and an experimental one named the GOES+NVI (C13+C14). This product used 15 inputs and ABI channel 13 and channel 14 combinations as well as channel 13-14, instead of just one of these bands and its BTDs. This was done as a test to see if more inputs improve the product given that the inputs are similar. As seen in the imagery, the difference between the two is most apparent in the contrast of low cloud versus ocean to the right of Otis but also obvious in some of the layered cloud in the northwest and south east sectors relative to storm center. Depending on the features one is observing, there may be benefit to one product over the other. This set also demonstrated that when clouds become denser, as often seen in hurricanes, they can become too dense to see the lower-level clouds unless there is shear causing

the vortex to become displaced. This product is best used with cyclones in shear or the formation levels before dense overcast is present.

These examples show additional benefits and identification of circulation and vertical structure and extent of the storm that A-NVI can provide forecasters over IR and the timing of the storm status changes may have been different to the update periods with this data. While the storm tracked outside of the view of the GOES 16 CONUS sector, GOES 17 full disk imagery could still provide 10 minute updates to the night visible imagery. If forecasters had access to this data, the timing and location of the low-level and mid level circulations as well as the tilting of the vortex would have been more apparent.

4.3.2 Fog

Bispectral differencing in the IR has been the foundation for nighttime cloud detection for decades but it is not without its own issues. The spatial distribution and depth of stratus combined with the type of fog (radiation, advection, etc) are key to predicting when fog may occur over an area. Imagery that can enhance the identification for these features will improve forecasts. Miller et al. (2022) demonstrated that DNB can help minimize false alarms in the nighttime marine boundary layer cloud detection algorithms and provide a better assessment of low cloud at night when combined with IR techniques. Hu et al. (2017) created a multichannel threshold algorithm (MRCT) that uses DNB TOA lunar reflectance and IR differences for low-cloud detection at night. They highlight that it is only useful for half the lunar phase since it requires (Miller and Turner, 2009) lunar reflectance. In addition to the imagery itself, NVI could enable these assessments as well as other night time products to occur more frequently over larger regions and for the full lunar cycle.

The fog case is an example of both radiation and advection fog in California from January 28, 2023 when there was approximately 48% lunar illumination. The event was tracked from approximately sunset to sunrise (28/02-16Z) though images selected all represent periods or darkness. The radiation fog occurs in the California valley and the advection fog is seen along the coast. For

the study all available imagery products for this archived period available from the CIRA/RAMMB slider (https://rammb-slider.cira.colostate.edu/) were explored but imagery for display was chosen from the mesoscale sector. In this forecasting situation, VIIRS NCC and radiances are available, but a forecaster would only have 1-2 images near 0130L /0930Z for nighttime visible imagery and the associated lunar reflectance imagery is at marginal production based on the illumination percentage. Current geostationary nighttime visible imagery from the GOES ABI sensors is only available for the full disk limiting temporal resolution to 10 minutes. A-NVI can be produced on mesoscale views providing 1 minute temporal resolution if required.

Figure 4.3 shows a map of the area of focus and the locations of 7 weather stations of interest. The bottom half of the figure highlights the aviation flight rules category that were observed and are divided by visibility and ceilings. Only one of the thresholds (visibility or ceilings) has to be met and it is the lower of the two that determines the category. Figure 4.4 shows three sets of six product images for 28/03, 28/06Z, and 28/15Z respectively. Each set has two infrared bands: ABI channel 07 (3.9 μm) and ABI enhanced channel 15 (12.3 μm) in the top left and top center, two split (10.3 μm -12.3 μm) window differences: grey (top right) and color enhanced (bottom right), the GeoColor multispectral imagery (lower left), and the A-NVI (center bottom). In many of the level 2 products not present, the ocean fog appears to be a single layer due to the embedded binning criteria. For the level 1 products we can do a better comparison of visualization. Starting at the top left of each set in ABI channel 07 (3.9 μm), cold cirrus clouds appear to the viewer as black and the extensive single looking layer of darker grey is the fog. ABI channel 15 (12.3 μm) in the middle top is great for identifying cirrus but not very helpful for the low clouds and demonstrates the minimal thermal contrast often present between land, low clouds, and ocean. The lack of contrast makes borders difficult to distinguish. On the far right, both split window techniques are displaying the same information but with and without an enhancement to assist forecaster visualization. Above the cirrus clouds, there appear white and low dark clouds that are more clearly distinguishable than the single IR channels alone. This can be confusing for a forecaster as some clouds are white and others are not. In the enhancement, both clear skies and cirrus can appear green which can be

misleading for some users while surface clouds appear blue. The GeoColor in the lower left is a very popular multispectral imagery product. Using the RGB concept and layering it combines a cold cloud enhanced IR, the 10.3 µm - 3.9 µm BTD for low cloud at night detection, and a surface with night lights from annual clear sky day night band (Miller et al., 2020). This is one of the most intuitive of the currently available products for fog forecasters. The low clouds appear blue while the cirrus is black. This imagery has the most contextual information of any of the current products and is it fairly easy to track the clouds over the open ocean. Identification can be more challenging over the land due to the saturation from city lights. This is the only image of current operational use that the valley fog can be easily detected in as the case progresses. In the A-NVI the first thing that is striking is how the open ocean fog appears white as it would in the visible imagery. This contrast is especially striking in comparison to IR imagery. Additionally, the A-NVI can capture the fog in the valley as it transitions from north to south as seen in the surface observations of Figure 4.3. Comparisons between the IR imagery and the NVI show that the fog appears to be a single layer in the IR,but looking at the A-NVI, it is actually more patchy than assumed by the IR. The A-NVI provides insight to the forecaster for texture and spatial distribution that is lacking in the IR and most level 2 products.

These two cases demonstrate that geostationary A-NVI can enhance a forecaster's awareness on developing phenomena and enable them to make a more informed forecast. So often the first light imagery for tropical storms or fog is when significant changes to observation and forecasts are made, but with nighttime visible imagery such as NVI we can help to minimize so much "sunrise surprise" fog and unexpected storm strengthening or position seen with the first daylight imagery products not captured in IR. Between these and other uses mentioned, the A-NVI will further close the gap between the known and unknown on nighttime clouds for forecasters and researchers.

4.4 Conclusions and Future Work

Satellite imagery and its increasing availability in temporal, spectral, and spatial resolution has greatly advanced the skill of forecasting meteorological events. Cloud identification by the human

eye is most easily done in the visible spectrum, but this is limited to daylight hours. The JPSS DNB provides a capability similar to traditional visible imagery at night using lunar reflectance and ambient light, however its limited sampling from polar orbiting satellites greatly limits its impact on short term forecasters. Other scientists have attempted to create a low-light visible product with varying levels of success, demonstrating the need of such a product (Chirokova et al., 2018; Kim and Hong, 2019; Kim et al., 2019, 2020; Mohandoss et al., 2020; Harder et al., 2020; Pasillas et al., 2023). ML-NVI is our solution to the remote sensing low-light visible problem.

The ML-NVI was created using a Fully connected Neural Network (FNN) and validated for use on both JPSS and ABI sensors as V-NVI and A-NVI respectively. Qualitative assessments demonstrated that it performs superior to single channel IR for the detection of low cloud at night, seeing through but not eliminating the appearance of cirrus, and appears similar to day night band imagery for user inferences. The product showed efficacy and visual consistency across all lunar phases and seasons extending the use period for DNB radiances in visual imagery. NVI imagery as is, can be incorporated in to a weather forecaster's tool box, providing an imagery product that will give additional insight to the current environment. This projected proved that with the NVI, knowledge of the fog life cycle and tropical cyclone center storm position identification are greatly enhanced for forecasters. NVI imagery can be incorporated into current cyclone center positioning algorithms and updated centers increase the accuracy of many aspects of tropical cyclone forecast. It may also improve understanding of the diurnal cloud cycle and global cloud climatologies which are critical to understanding the Earth's radiation budget. The knowledge gained from updating the diurnal, seasonal, and annual cloud data may lead to updated ISCCP/GEWEX cloud climatologies. As more clouds can be detected in NVI, it provides a new input source in cloud tracking for atmospheric motion vectors and optical flow algorithms. New knowledge on global wind flow can thus improve forecasting of steering flow, wind speeds and circulation patterns of tropical cyclones as well as identify open ocean winds which may influence fog development and dissipation.

This dissertation provided the first documented quantitative validation for nighttime visual imagery against DNB measurements and stands as the benchmark for future models. Though statistics

were much higher in the VIIRS generated NVI data sets, quantitative validation of the model for both VIIRS (Chapter 2) and ABI (Chapter 3) sensors demonstrates good explained variance and correlation values between model derived lunar reflectance and lunar reflectance values calculated from direct satellite measurements at full moon. This demonstrates that wavelength and radiative transfer theory can explain the preponderance of similarities in the visualization of clouds at night using lunar reflectance whether from direct measurements of the DNB radiances or through transforms of IR measurements. Because the NVI calculates a lunar reflectance value derived directly from satellite retrieved radiances, it can be used to assist in nighttime optical depth calculations and cloud height assignment. Based on the Jensen Shannon Divergence scores, calculated lunar reflectance can be used as a substitution in many applications and level 2 products that the DNB and DNB lunar reflectance are currently a part of to include multispectral imagery, algorithms, and model forecasting.

It is possible there is a more ideal combination of ABI channels for low-cloud detection than what the A-NVI provides that still behaves as visible imagery. Investigating other channel combinations or including other parameters such as sea surface temperature or satellite viewing angle was beyond the scope of this project, but future work should explore utilizing all ABI channels or providing a baseline or mean background scene value for clear sky radiances and testing against VIIRS lunar reflectance. This could be done with the same baseline model concept but adjusting inputs accordingly to account for varying wavelengths and the number of predictors. It was beneficial to have the large land free region of the Pacific Ocean for validation and future models should utilize data from GOES 18 (unavailable at time of this study) to avoid GOES 17 heat loop pipe issues. They can consider a larger AOI with data from the southern hemisphere as well.

Image styling, convolutional neural networks (CNNs), and UNets show great promise in morphing images to look like training data sets while conditional generative adversarial networks (CGANs) can replicate imagery. A FNN only accounts for pixel analysis but forecasters often use spatial context and patterns to aid in cloud identification with imagery. Because of this, further explorations in AI-ML should include CNN or CGANS to account for spatial distribution and

relationships between pixels at varying scales. Addressing both channels and spatial relationships will help to achieve the most accurate combination that retains visual satellite image qualities and enhances low cloud identification at night and one can expect higher explained variance, variance, and correlation metrics reflecting this. Additionally, future research should include the operationalization and inclusion of the NVI product on the varied platforms weather forecasters use for further application testing.

Both the V-NVI and A-NVI products demonstrate high skill in low-cloud detection and the benefits to operational weather forecasting world and research community are plentiful. Providing forecasters the capability to perceive clouds at night, as they do during the daytime, will greatly improve short-to-medium range forecasting, especially of hazardous meteorological phenomena such as low-lying stratus and tropical cyclones and will enhance the forecasters ability to detect clouds and hazards in real time capabilities across the globe at night, enhancing safety for flight operations and the general populous. The NVI represents a viable solution to the low-light visibility problem until the community can develop and fund a new sensor capability on geostationary orbiters or low Earth orbiting small sat constellations.

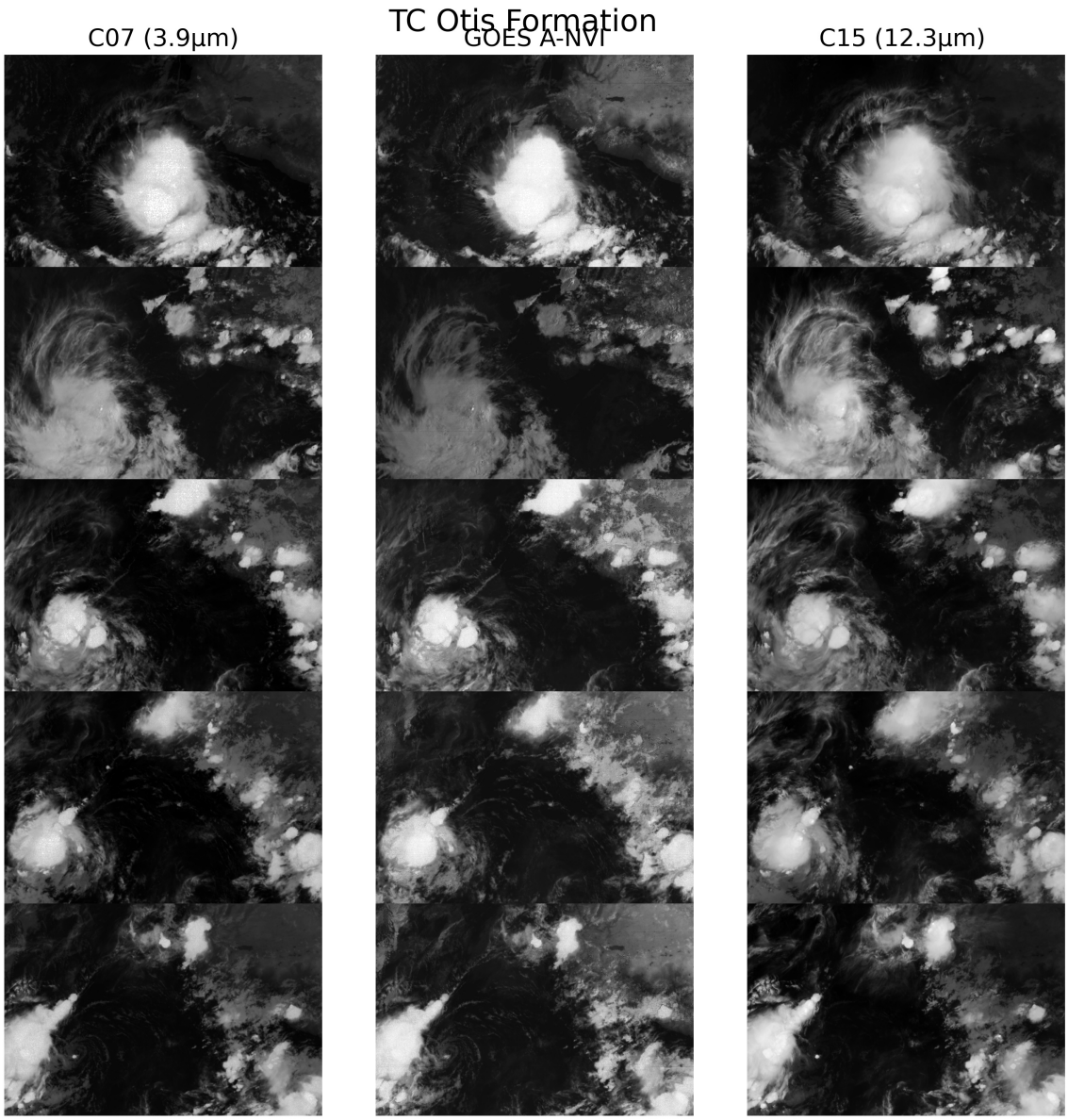

Figure 4.1: Hurricane Otis comparisons of ABI channel C07 (3.9µm), A-NVI, and ABI channel C15 (12.3µm)(left to right) leading to tropical depression declaration at times 10/12Z 11/00Z 11/03Z/ 11/06Z and 11/09Z (top to bottom)

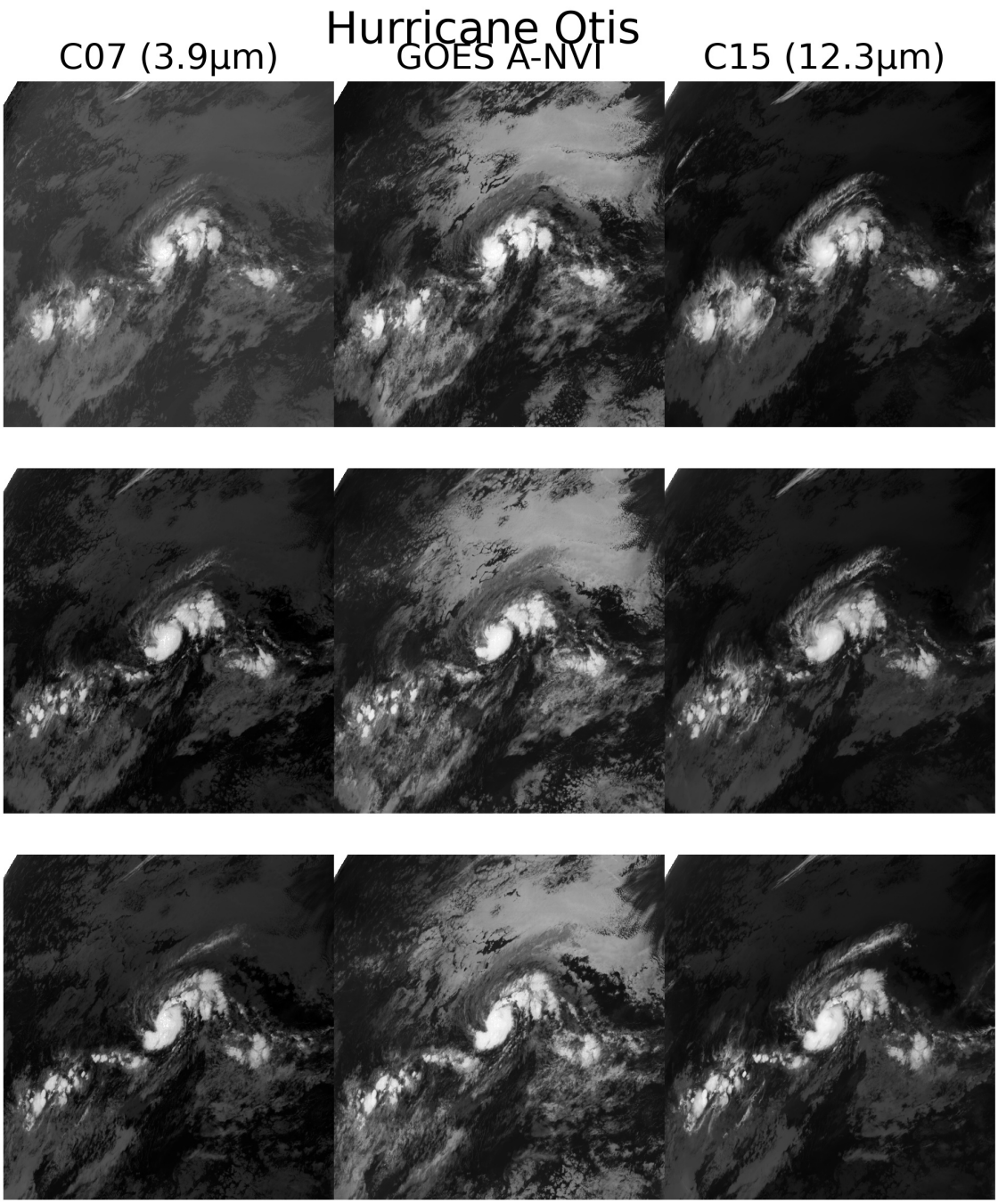

Figure 4.2: Hurricane Otis comparisons of ABI channel C07 (3.9 µm), C13 A-NVI, GOES+ A-NVI and ABI channel C15 (12.3 µm) (left to right) at times 17/04Z, /17/07Z, and 17/10Z (top to bottom) leading to category 1 hurricane declaration.

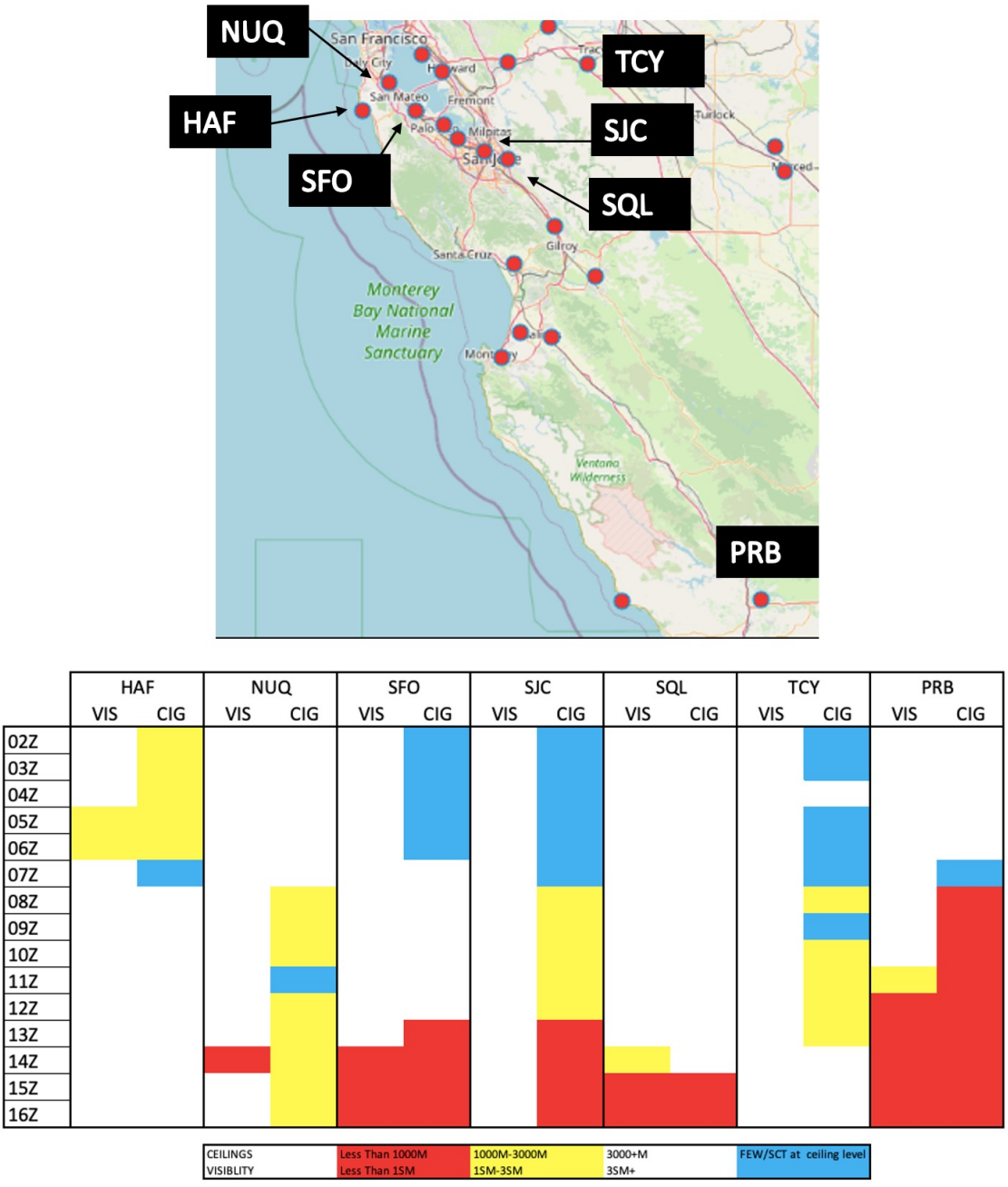

Figure 4.3: Map of the sensor locations in the area of interest (top) and ceiling and visible coding for Instrument Flight Rules (red), Marginal Visual Flight Rules (yellow), Visual Flight Rules (white), and potential M/IFR (blue) observations by hour from 02Z-16Z for the event.)

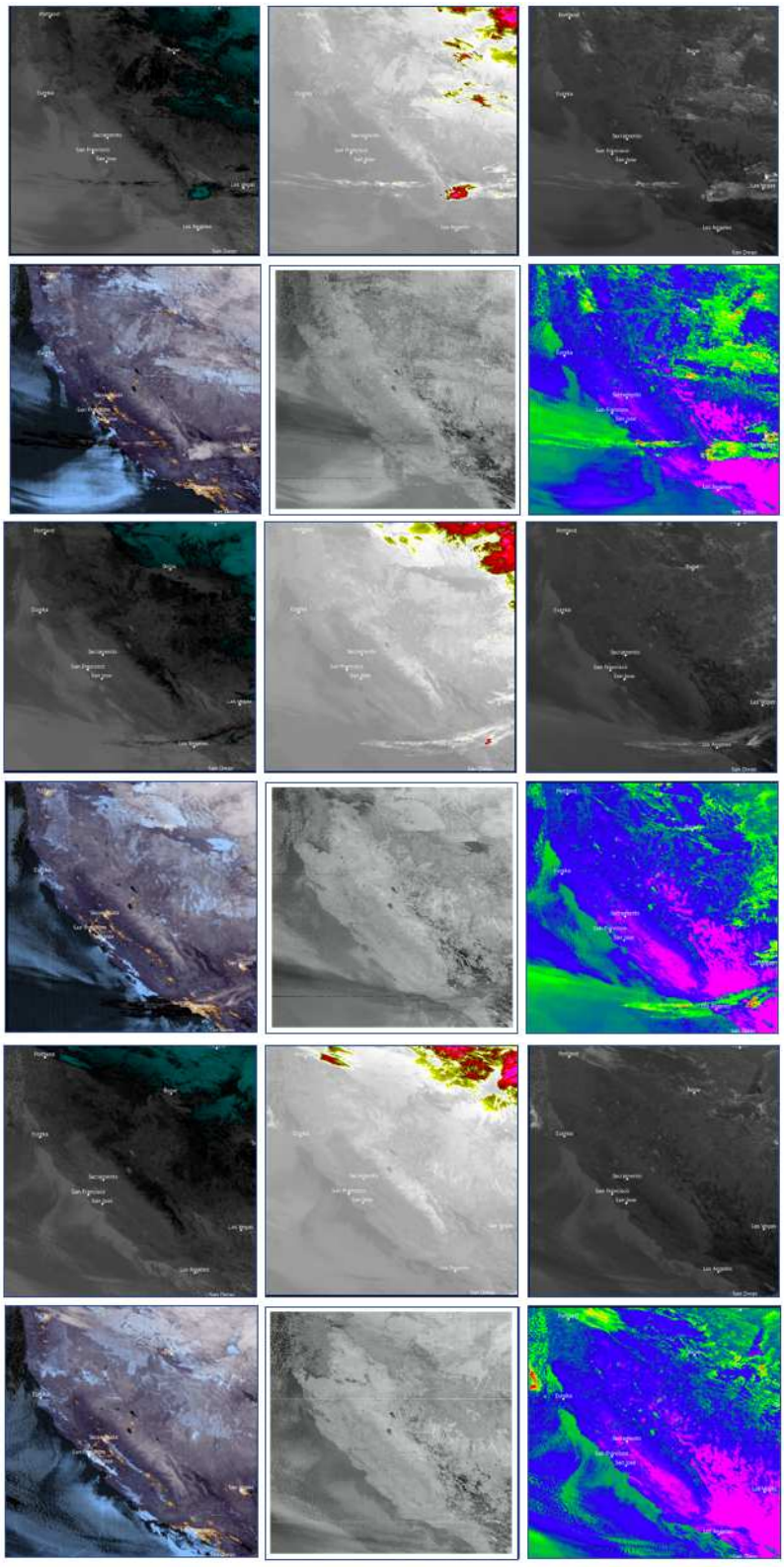

Figure 4.4: Comparisons for 28 January 2023 fog case at 03Z (top set), 09Z (middle set), and 15Z (bottom set) for A-NVI and current forecasting imagery.)

Bibliography

Baker, N., 2013: Joint polar satellite system (JPSS) viirs radiometric calibration algorithm theoretical basis document (atbd). ATBD C, NASA, 197 pp.

Bendix, J., 2002: A satellite-based climatology of fog and low-level stratus in germany and adjacent areas. *Atmospheric Research*, **64**, 3–18, doi: 10.1016/S0169-8095(02)00075-3.

Calvert, C., and M. Pavolonis, 2010: GOES-R advanced baseline imager (ABI) algorithm theoretical basis document ATBD for low cloud and fog. ATBD 1, NOAA-NESDIS, 78 pp.

Carlomusto, M., 2019: GOES Product User Guide PUG volume 3:Level 1b Products. Tech. rep., Harris Cooperation.

Cermak, J., and J. Bendix, 2005: Fog/low stratus detection and discrimination using satellite data. *Short range forecasting methods of fog, visibility and low clouds*, 50.

Chander, G., T. J. Hewison, N. Fox, X. Wu, X. Xiong, and W. J. Blackwell, 2013: Overview of intercalibration of satellite instruments. *IEEE Transactions on Geoscience and Remote Sensing*, **51 (3)**, 1056–1080, doi: 10.1109/TGRS.2012.2228654.

Chapman, R., and R. Gasparovic, 2022: *Remote Sensing Physics: An Introduction to Observing Earth from Space*. John Wiley & Sons.

Cheng, W., Q. Li, Z. Wang, W. Zhang, and F. Huang, 2022: Creating synthetic night-time visible-light meteorological satellite images using the gan method. *Remote Sensing Letters*, **13 (7)**, 738–745, doi: DOI:10.1080/2150704X.2022.2079016.

Chirokova, G., J. A. Knaff, and J. L. Beven, 2018: Proxy visible satellite imagery. *Proc. 22nd Conference on Satellite Meteorology and Oceanography*, Austin, Texas, Amer. Meteor. Soc., 7.6, URL https://ams.confex.com/ams/98Annual/webprogram/Paper334276.html.

Davis, G. K., 2007: History of the NOAA satellite program. *Journal of Applied Remote Sensing*, **1 (1)**, 012 504.

Dvorak, V. F., 1984: Tropical cyclone intensity analysis using satellite data tech. rep. 11. Tech. rep., NOAA, 45 pp.

Ellrod, G. P., 1995: Advances in the detection and analysis of fog at night using GOES multispectral infrared imagery. *Weather and Forecasting*, **10 (3)**, 606–619.

Ellrod, G. P., 2002: Estimation of low cloud base heights at night from satellite infrared and surface temperature data. *National Weather Digest*, **26 (1/2)**, 39–44.

EUMETSAT, 2010: Atbd for prototype gsics seviri-iasi inter-calibration. Tech. rep., EUMETSAT.

Fiore, J., and M. Seybold, 2021: Addendum to goes-17 saturation prediction reference tools for 2021. Tech. rep., NOAA - NASA.

Greenfield, S., and W. Kellogg, 1960: Inquiry into the feasibility of weather reconnaissance from a satellite vehicle. *Exploring Unknown*, 184.

Gunshor, M. M., T. J. Schmit, and W. P. Menzel, 2004: Intercalibration of the infrared window and water vapor channels on operational geostationary environmental satellites using a single polar-orbiting satellite. *Journal of Atmospheric and Oceanic Technology*, **21 (1)**, 61 – 68, doi: 10.1175/1520-0426(2004)021<0061:IOTIWA>2.0.CO;2, URL https://journals.ametsoc.org/view/journals/atot/21/1/1520-0426_2004_021_0061_iotiwa_2_0_co_2.xml.

Gurka, J. J., 1978a: The role of inward mixing in the dissipation of fog and stratus. *Monthly Weather Review*, **106 (11)**, 1633–1635.

Gurka, J. J., 1978b: The use of enhanced visible imagery for predicting the time of fog dissipation. *Conference on weather forecasting and analysis and aviation meteorology. NOAA, Washington, DC, USA*, 343–346.

Harder, P., and Coauthors, 2020: Nightvision: Generating nighttime satellite imagery from infrared observations. *arXiv preprint arXiv:2011.07017*.

Hawkins, J. D., J. E. Solbrig, S. D. Miller, M. Surratt, T. F. Lee, R. L. Bankert, and K. Richardson, 2017: Tropical cyclone characterization via nocturnal low-light visible illumination. *Bulletin of the American Meteorological Society*, **98 (11)**, 2351 – 2365, doi: 10.1175/BAMS-D-16-0281.1, URL https://journals.ametsoc.org/view/journals/bams/98/11/bams-d-16-0281.1.xml.

Herndon, D., T. Wimmers, T. Olander, and C. Velden, 2021: Uw-cimss products for tc centering, intensity and structure. *2021 RA-IV WMO Workshop on Hurricane Forecasting and Warning*, URL https://severeweather.wmo.int/TCFW/RAIV_Workshop2021/11_UW-CIMSSProducts_DerrickHerndon.pdf.

Hillger, D., and Coauthors, 2016: User validation of viirs satellite imagery. *Remote Sensing*, **8 (1)**, doi: 10.3390/rs8010011, URL https://www.mdpi.com/2072-4292/8/1/11.

Hillger, D. W., 2008: GOES-R advanced baseline imager color product development. *Journal of Atmospheric and Oceanic Technology*, **25 (6)**, 853–872.

Hogan, R. J., E. J. O'Connor, and A. J. Illingworth, 2009: Verification of cloud-fraction forecasts. *Quarterly Journal of the Royal Meteorological Society: A journal of the atmospheric sciences, applied meteorology and physical oceanography*, **135 (643)**, 1494–1511.

Hopkins, E., 2004: Atmospheric and ocean sciences 100: Weather and climate. lecture notes. *Proc. 22nd Conference on Satellite Meteorology and Oceanography Amer. Meteor. Soc.*, URL http://www.aos.wisc.edu/~hopkins/wx-inst/satpltfm.htm, accessed Dec 2019.

Hu, S., S. Ma, W. Yan, J. Jiang, and Y. Huang, 2017: A new multichannel threshold algorithm based on radiative transfer characteristics for detecting fog/low stratus using night-time npp/viirs data. *International Journal of Remote Sensing*, **38 (21)**, 5919–5933, doi: 10.1080/01431161.2016.1265691, URL https://doi.org/10.1080/01431161.2016.1265691, https://doi.org/10.1080/01431161.2016.1265691.

Huang, J., B. Yan, and N. Sun, 2020: Monitoring of the cross-calibration biases between the s-npp and noaa-20 viirs sensor data records using goes advanced baseline imager as a transfer. *IGARSS 2020 - 2020 IEEE International Geoscience and Remote Sensing Symposium*, 6393–6396, doi: 10.1109/IGARSS39084.2020.9323300.

Huang, Q., X. Yang, B. Gao, Y. Yang, and Y. Zhao, 2014: Application of dmsp/ols nighttime light images: A meta-analysis and a systematic literature review. *Remote Sensing*, **6 (8)**, 6844–6866.

Inoue, T., 1989: Features of clouds over the tropical pacific during northern hemispheric winter derived from split window measurements. *Journal of the Meteorological Society of Japan*.

JTWC, 2018: Joint typhoon warning center JTWC general standard operating procedure 06a fix procedures and 06b dvorak technique. Tech. rep., Joint Typhoon Warning Center.

Kidder, S. Q., D. W. Hillger, A. J. Mostek, and K. J. Schrab, 2000: Two simple GOES imager products for improved weather analysis and forecasting. *National Weather Digest*, **24:4**, 25–30, doi: 10.1080/01431169921287.

Kidder, S. Q., and T. H. Vonder Haar, 1995: *Satellite Meteorology: an Introduction*. Gulf Professional Publishing.

Kieffer, H. H., and T. C. Stone, 2005: The spectral irradiance of the moon. *The Astronomical Journal*, **129 (6)**, 2887.

Kim, J.-H., S. Ryu, J. Jeong, D. So, H.-J. Ban, and S. Hong, 2020: Impact of satellite sounding data on virtual visible imagery generation using conditional generative adversarial network. *IEEE Journal of Selected Topics in Applied Earth Observations and Remote Sensing*, **13**, 4532–4541, doi: 10.1109/JSTARS.2020.3013598.

Kim, K., J.-H. Kim, Y.-J. Moon, E. Park, G. Shin, T. Kim, Y. Kim, and S. Hong, 2019: Nighttime reflectance generation in the visible band of satellites. *Remote Sensing*, **11 (18)**, 2087.

Kim, Y., and S. Hong, 2019: Deep learning-generated nighttime reflectance and daytime radiance of the midwave infrared band of a geostationary satellite. *Remote Sensing*, **11 (22)**, 2713.

Lee, S. J., and M.-H. Ahn, 2021: Synergistic benefits of intercomparison between simulated and measured radiances of imagers onboard geostationary satellites. *IEEE Transactions on Geoscience and Remote Sensing*, **59 (12)**, 10 725–10 737, doi: 10.1109/TGRS.2021.3054030.

Lee, T. E., S. D. Miller, F. J. Turk, C. Schueler, R. Julian, S. Deyo, P. Dills, and S. Wang, 2006: The NPOESS VIIRS day/night visible sensor. *Bulletin of the American Meteorological Society*, **87 (2)**, 191–200.

Levin, N., and Coauthors, 2020: Remote sensing of night lights: A review and an outlook for the future. *Remote Sensing of Environment*, **237 (111443)**, doi: doi.org/10.1016/j.rse.2019.111443.

Liang, C. K., S. Mills, B. I. Hauss, and S. D. Miller, 2014: Improved VIIRS day/night band imagery with near-constant contrast. *IEEE Transactions on Geoscience and Remote Sensing*, **52 (11)**, 6964–6971.

Lin, L., and C. Cao, 2019: The effects of VIIRS detector-level and band-averaged relative spectral response differences between s-npp and noaa-20 on the thermal emissive bands. *IEEE Journal of Selected Topics in Applied Earth Observations and Remote Sensing*, **12 (10)**, 4123–4130.

Line, B., D. Hillger, and T. Kopp, 2018: Joint polar satellite system (JPSS) VIIRS imagery products algorithm theoretical basis document (ATBD) revision E. ATBD, NOAA NESDIS CENTER for SATELLITE APPLICATIONS and RESEARCH, 55 pp.

Liou, K.-N., 2002: *An Introduction to Atmospheric Radiation*, Vol. 84. Elsevier.

Loew, A., and Coauthors, 2017: Validation practices for satellite-based earth observation data across communities. *Reviews of Geophysics*, **55 (3)**, 779–817.

McCormack, N., 2019: The rescue of apollo 11. *National Reconnaissance Office News*, URL https://www.nro.gov/News-and-Media/Article/1906117/the-rescue-of-apollo-11/.

Miller, S. D., J. D. Hawkins, K. Richardson, T. F. Lee, and F. J. Turk, 2006: Enhanced tropical cyclone monitoring with MODIS and OLS. *Proc. 27th Hurr. Trop. Meteor. Conf. Amer. Meteor. Soc.*

Miller, S. D., D. T. Lindsey, C. J. Seaman, and J. E. Solbrig, 2020: Geocolor: A blending technique for satellite imagery. *Journal of Atmospheric and Oceanic Technology*, **37 (3)**, 429 – 448, doi: 10.1175/JTECH-D-19-0134.1, URL https://journals.ametsoc.org/view/journals/atot/37/3/JTECH-D-19-0134.1.xml.

Miller, S. D., and R. E. Turner, 2009: A dynamic lunar spectral irradiance data set for NPOESS/VIIRS day/night band nighttime environmental applications. *IEEE Transactions on Geoscience and Remote Sensing*, **47 (7)**, 2316–2329.

Miller, S. D., and Coauthors, 2013: Illuminating the capabilities of the suomi national polar-orbiting partnership (NPP) visible infrared imaging radiometer suite (VIIRS) day/night band. *Remote Sensing*, **5 (12)**, 6717–6766.

Miller, S. D., and Coauthors, 2022: A physical basis for the overstatement of low clouds at night by conventional satellite infrared-based imaging radiometer bi-spectral techniques. *Earth and Space Science*, **9 (2)**, e2021EA002 137.

Min, M., and Coauthors, 2017: An investigation of the implications of lunar illumination spectral changes for day/night band-based cloud property retrieval due to lunar phase transition. *Journal of Geophysical Research: Atmospheres*, **122 (17)**, 9233–9244.

Mohandoss, T., A. Kulkarni, D. Northrup, E. Mwebaze, and H. Alemohammad, 2020: Generating synthetic multispectral satellite imagery from Sentinel-2. *arXiv preprint arXiv:2012.03108*.

Pasillas, C., C. Kummerow, M. Bell, and S. D. Miller, 2023: Turning night into day: The creation and validation of synthetic night-time visible imagery using the joint polar satellite system (jpss) day-night band (dnb) and machine learning. *Artificial Intelligence for the Earth Systems*.

Petty, G. W., 2006: *A First Course in Atmospheric Radiation*. Sundog Pub.

Pitts, K., and M. Seybold, 2010: Abi l2 cloud and moisture imagery beta, provisional and full validation readiness, implementation and management plan (RIMP) V2. 410-R-RIMP-0323 2, NOAA-NESDIS, 31 pp.

PyTroll, 2009-2022: Satpy. Tech. rep., PyTroll Team. URL https://satpy.readthedocs.io/en/stable/overview.html.

Schmit, T. J., P. Griffith, M. M. Gunshor, J. M. Daniels, S. J. Goodman, and W. J. Lebair, 2017: A closer look at the ABI on the GOES-R series. *Bulletin of the American Meteorological Society*, **98 (4)**, 681–698, doi: 10.1175/BAMS-D-15-00230.1, URL https://journals.ametsoc.org/view/journals/bams/98/4/bams-d-15-00230.1.xml.

Schultz, D. M., 2010: How to research and write effective case studies in meteorology. *Electronic J. Severe Storms Meteor.*, **5 (2)**, 1–18, URL https://ejssm.org/archives/wp-content/uploads/2021/09/vol5-2.pdf.

Seaman, C., D. W. Hillger, T. J. Kopp, R. Williams, S. Miller, and D. Lindsey, 2015: Visible infrared imaging radiometer suite (VIIRS) imagery environmental data record (EDR) user's guide version 1.3. Technical Report NOAA technical report NESDIS ; 150, NOAA-NESDIS, 55 pp. doi: 10.7289/V5/TR-NESDIS-150.

Seaman, C. J., and S. D. Miller, 2015: A dynamic scaling algorithm for the optimized digital display of VIIRS day/night band imagery. *International Journal of Remote Sensing*, **36 (7)**, 1839–1854.

Stephens, G. L., 1994: *Remote Sensing of the Lower Atmosphere: An Introduction*. Oxford University Press.

Strabala, K. I., S. A. Ackerman, and W. P. Menzel, 1994: Cloud properties inferred from 8–12-μm data. *Journal of Applied Meteorology and Climatology*, **33 (2)**, 212–229, doi: 10.1175/1520-0450(1994)033<0212:CPIFD>2.0.CO;2.

Suomi, V. E., and R. J. Parent, 1968: A color view of planet earth. *Bulletin of the American Meteorological Society*, **49 (2)**, 74–75.

Vaughn, 1982: Meteorological satellites-past,present, and future. *Proceedings of the session on Meteorological Satellites at AIAA 20th Aerospace Sciences Meeting*, NASA, 69.

Velden, C., and Coauthors, 2006: The dvorak tropical cyclone intensity estimation technique: A satellite-based method that has endured for over 30 years. *Bulletin of the American Meteorological Society*, **87 (9)**, 1195 – 1210, doi: 10.1175/BAMS-87-9-1195, URL https://journals.ametsoc.org/view/journals/bams/87/9/bams-87-9-1195.xml.

Velden, C. S., 2020: Chapter 9 - goes-r series applications to hurricane monitoring. *The GOES-R Series*, S. J. Goodman, T. J. Schmit, J. Daniels, and R. J. Redmon, Eds., Elsevier, 95–102, doi: https://doi.org/10.1016/B978-0-12-814327-8.00009-3, URL https://www.sciencedirect.com/science/article/pii/B9780128143278000093.

Warren, S. G., C. J. Hahn, J. London, R. M. Chervin, R. L. Jenne, C. Colorado Univ., Boulder, C. Colorado Univ., Boulder, and C. National Center for Atmospheric Research, Boulder, 1988: Global distribution of total cloud cover and cloud type amounts over the ocean. Technical Report, USDOE Office of Energy Research, Washington, DC (USA). Carbon Dioxide Research Div.; National Center for Atmospheric Research, Boulder, CO (USA), 305 pp. doi: 10.2172/5415329, URL https://www.osti.gov/biblio/5415329.

Weiss, M., 2001: Avn-based MOS ceiling height and total sky cover guidance for the contiguous united states, alaska, hawaii and puerto rico. Technical Procedure Bulletin 483, National Weather Service, 22 pp.

Wimmers, A. J., and C. S. Velden, 2016: Advancements in objective multisatellite tropical cyclone center fixing. *Journal of Applied Meteorology and Climatology*, **55 (1)**, 197–212, doi: 10.1175/JAMC-D-15-0098.1, URL https://journals.ametsoc.org/view/journals/apme/55/1/jamc-d-15-0098.1.xml.

Yu, F., X. Wu, H. Yoo, H. Quan, X. Shao, Z. Wang, and R. Iacovazzi, 2021: Radiometric calibration accuracy and stability of goes-16 abi infrared radiance. *J. Appl. Rem. Sens.*, **15 (4)**, doi: 10.1117/1.JRS.15.048504.

Zhongming, Z., L. Linong, Y. Xiaona, Z. Wangqiang, L. Wei, and Coauthors, 2012: Recommended methods for evaluating cloud and related parameters. Technical Report WWRP- No. 2012-1, WMO, 305 pp.

Zinke, S., 2017: A simplified high and near-constant contrast approach for the display of viirs day/night band imagery. *International Journal of Remote Sensing*, **38 (19)**, 5374–5387.